

# Short-Term Interaction between Silent and Devastating Earthquakes in Mexico

Víctor Cruz-Atienza (✉ [cruz@geofisica.unam.mx](mailto:cruz@geofisica.unam.mx))

Instituto de Geofísica, Universidad Nacional Autónoma de México <https://orcid.org/0000-0001-7067-2636>

Josué Tago

Facultad de Ingeniería, Universidad Nacional Autónoma de México

Carlos Villafuerte

Instituto de Geofísica, UNAM <https://orcid.org/0000-0003-1539-3751>

Meng Wei

Graduate School of Oceanography, University of Rhode Island

Ricardo Garza-Girón

Department of Earth and Planetary Sciences, University of California

Luis Dominguez

Escuela Nacional de Estudios Superiores, Universidad Nacional Autónoma de México

Vladimir Kostoglodov

Instituto de Geofísica, Universidad Nacional Autónoma de México

Takuya Nishimura

Geospatial Information Authority of Japan <https://orcid.org/0000-0002-2469-8146>

Sara Franco

Instituto de Geofísica, Universidad Nacional Autónoma de México

Jorge Real

Instituto de Geofísica, Universidad Nacional Autónoma de México

Miguel Santoyo

Instituto de Geofísica, Universidad Nacional Autónoma de México

Yoshihiro Ito

Disaster Prevention Research Institute, Kyoto University

Ekaterina Kazachkina

Instituto de Geofísica, Universidad Nacional Autónoma de México

---

## Article

**Keywords:** earthquakes, slow slip events, seismic waves, large populated areas, Mexico

**Posted Date:** August 24th, 2020

**DOI:** <https://doi.org/10.21203/rs.3.rs-59956/v1>

**License:**  This work is licensed under a Creative Commons Attribution 4.0 International License.

[Read Full License](#)

---

**Version of Record:** A version of this preprint was published at Nature Communications on April 12th, 2021. See the published version at <https://doi.org/10.1038/s41467-021-22326-6>.

1  
2  
3  
4  
5  
6  
7  
8  
9  
10  
11  
12  
13  
14  
15  
16  
17

# Short-Term Interaction between Silent and Devastating Earthquakes in Mexico

**Authors:** V. M. Cruz-Atienza<sup>1\*</sup>, J. Tago<sup>2</sup>, C. Villafuerte<sup>3</sup>, M. Wei<sup>4</sup>,  
R. Garza-Girón<sup>5</sup>, L. A. Dominguez<sup>6</sup>, V. Kostoglodov<sup>1</sup>, T. Nishimura<sup>7</sup>,  
S. I. Franco<sup>1</sup>, J. Real<sup>1</sup>, M. A. Santoyo<sup>1</sup>, Y. Ito<sup>7</sup> and E. Kazachkina<sup>3</sup>.

## Affiliations

- <sup>1</sup>Instituto de Geofísica, Universidad Nacional Autónoma de México, Mexico City, Mexico.
- <sup>2</sup>Facultad de Ingeniería, Universidad Nacional Autónoma de México, Mexico City, Mexico.
- <sup>3</sup>Posgrado en Ciencias de la Tierra, Universidad Nacional Autónoma de México, Mexico City, Mexico.
- <sup>4</sup>Graduate School of Oceanography, University of Rhode Island, USA.
- <sup>5</sup>Department of Earth and Planetary Sciences, University of California, Santa Cruz, USA.
- <sup>6</sup>Escuela Nacional de Estudios Superiores, Universidad Nacional Autónoma de México, Mexico.
- <sup>7</sup>Disaster Prevention Research Institute, Kyoto University, Japan.

\*Correspondence to: [cruz@geofisica.unam.mx](mailto:cruz@geofisica.unam.mx)

**August 2020**

1 **Abstract**

2 Triggering of large earthquakes on a fault that hosts aseismic slip or, conversely, triggering of slow  
3 slip events (SSE) by passing seismic waves involves seismological questions with major hazard  
4 implications. Just a few observations plausibly suggest that such interactions actually happen in  
5 nature. In this study we show that three recent devastating earthquakes in Mexico are likely related  
6 to SSEs, describing a cascade of events interacting with each other on a regional scale via quasi-  
7 static and/or dynamic perturbations. Such interaction seems to be conditioned by the transient  
8 memory of Earth materials subject to the “traumatic” stressing produced by the seismic waves of  
9 the great Mw8.2 Tehuantepec earthquake, which strongly disturbed the aseismic beating over a 650  
10 km long segment of the subduction plate interface. Our results imply that seismic hazard in large  
11 populated areas is a short-term evolving function of seismotectonic processes that are often  
12 observable.

13

14 **Introduction**

15 Seismicity rate varies over time and depends on changes in both the state of stress and properties of  
16 the solid Earth. The diversity of earthquakes discovered in recent years, together with new  
17 observations of very small transient variations in the crustal properties, offer an unprecedented  
18 perspective for exploring causality between different seismotectonic processes. Inferred effects of  
19 slow slip events (SSE, also called silent earthquakes) on large and devastating earthquakes have led  
20 to critical questions closely related to seismic hazard. The role of SSEs in the seismic cycle has been  
21 identified as preponderant in the initiation of some megathrust earthquakes (1-5). Observations also  
22 show that transient waves from teleseismic or regional earthquakes may trigger SSEs and tectonic  
23 tremor (6-10), which are two closely related phenomena in active faults. Highly pressurized fluids

1 where slow earthquakes happen (11) make frictional conditions very sensitive to small stress or  
2 strain perturbations (12, 13), thus playing an important role in the generation of slow earthquakes  
3 and, certainly, in their interaction with devastating events.

4 Recently, three major earthquakes took place in southcentral Mexico causing more than 480 deaths  
5 and losses for 1,6 billion dollars. The earthquake sequence initiated with the great Mw8.2  
6 Tehuantepec event on September 8, 2017, the largest earthquake ever recorded in Mexico, which  
7 may have broken the whole subducted Cocos lithosphere (14, 15) (Fig. 1). Eleven days later and  
8 480 km northwest, on September 19, the Mw7.1 Puebla-Morelos normal-faulting (57 km depth)  
9 event delivered a deadly shock to Mexico City (16), where 44 buildings collapsed and 600 were  
10 seriously damaged despite its remarkably slow, dissipative rupture (17). The sequence ended five  
11 months later on February 16, 2018, with a Mw7.2 thrust event below Pinotepa Nacional, Oaxaca  
12 (hereafter Pinotepa), more than 250 km away from both previous earthquakes, causing damage  
13 where similar ruptures have severely harmed local infrastructures in the past. Besides damaging  
14 earthquakes, the Mexican subduction zone is prone to very large SSEs and persistent tectonic  
15 tremor, especially in the Guerrero and Oaxaca states, which extend along the epicentral regions of  
16 the earthquake sequence (18-23). At the time of the Tehuantepec and Puebla-Morelos events, two  
17 separate SSEs were taking place in Guerrero and Oaxaca (23, 24). As we shall see, other SSEs also  
18 happened in both states in an unusual way during and after the five-month earthquake sequence,  
19 featuring a unique and fascinating story that deserves to be told and understood. In this work we  
20 investigate possible interactions between such SSEs and the three devastating earthquakes, and  
21 found that most of our observations can be explained as a regional cascade of causally related events  
22 through short-term, quasi-static and dynamic interactions that have strongly perturbed the regional  
23 plate-interface aseismic beating.

## 1 Results

### 2 • Plate Interface Aseismic Slip History

3 In the Mexican subduction zone, slow surface displacement can be explained in terms of the  
4 aseismic slip between the subducted Cocos plate and the overriding North American plate. Such  
5 slip can be understood either as SSEs, post-seismic relaxations or plate interface coupling (PIC, i.e.  
6  $1 - v / b$ , where  $v$  is the interplate slip rate,  $b$  is the plate convergence rate and  $v \leq b$ ). For imaging  
7 the spatial evolution of the aseismic slip in those terms, we inverted continuous displacement  
8 records at 57 permanent GPS stations from November 2016 to October 2019, the largest dataset  
9 ever analyzed in Mexico, making use of ELADIN, a recently developed and powerful technique  
10 (25) (Methods, Fig. S1). Careful examination of the GPS time series revealed several transient  
11 deformations in the Guerrero and Oaxaca states. Figure 2 presents the aseismic-slip inversion results  
12 for the whole analyzed period, where we find: (Fig. 2B) the 2017 Mw6.9 Guerrero SSE that reached  
13 shallow interface regions (up to 10 km depth, Fig. S2) and the initiation of the 2017 Mw6.9 Oaxaca  
14 SSE before the onset of the earthquake sequence; (Fig. 2B-2D) the evolution of the 2017 Mw6.9  
15 Oaxaca SSE; (Fig. 2E-2F) the Mw7.2 post-seismic slip of the Pinotepa earthquake that lasted at  
16 least until November 2018, together with a neighboring but separated, 200 km length, Mw6.9 SSE  
17 in Guerrero (second one); and (Fig. 2G-2H) the concomitant evolution of the 2019 Mw7.0 Guerrero  
18 (third one) and Mw6.9 Oaxaca (second one) SSEs (Table 1). The aseismic slip evolution for all  
19 analyzed windows is summarized in Figs. 1 and S2. Considering only the slip areas encompassed  
20 by 1 cm contours (Fig. 1), the aseismic moment released during this three-year period is equivalent  
21 to a magnitude Mw7.5 earthquake ( $M_0 = 2.32 \times 10^{20}$  Nw\*m), where only 31% of  $M_0$  corresponds  
22 to the post-seismic slip of the Mw7.2 Pinotepa rupture (Table 1).

1 Figure 3 shows the aseismic slip evolution (for events with  $M_w > 6$ ) throughout the period of the  
2 earthquake sequence. For the analysis, we separated the slip history in two parts; one before (Fig.  
3 3A) and the other after (Fig. 3B) the Pinotepa earthquake. The second part includes the previous  
4 inverted window as a reference. Panel A shows that the 2017 Guerrero SSE basically ended with  
5 the occurrence of the devastating Tehuantepec and Puebla-Morelos earthquakes. Only a few minor  
6 slip patches were imaged in the following three months (Fig. 2C). We further see that the 2017  
7 Oaxaca SSE, which also initiated months before the earthquakes, developed bilaterally during the  
8 five months that followed. More interestingly, examination of the GPS time series in the southern  
9 stations reveals a sudden reversal of the displacement direction from north to south (green circles,  
10 left) at the moment of the great Tehuantepec event. In contrast, northern stations (green circles,  
11 right) feature a slow, typical SSE initiation well before, around May-June 2017. The sharp change  
12 of the deformation regime in the south suggests that the Tehuantepec earthquake modified the  
13 ongoing Oaxaca SSE. In addition, the question arises as to whether the Guerrero and Oaxaca SSEs  
14 could have promoted the rupture of the Puebla-Morelos and Pinotepa earthquakes, respectively, as  
15 proposed for other earthquakes in Mexico (5, 21).

16 The GPS displacements in Panel B show a similar effect over the ongoing Oaxaca SSE to that  
17 inferred for the Tehuantepec earthquake, but in this case produced by the  $M_w 7.2$  Pinotepa event.  
18 While displacements in the eastern stations show either an ongoing or a smooth, spontaneously  
19 initiated SSE before this earthquake (green circles, right), some stations to the west exhibit again an  
20 abrupt change of displacements from north to south, right when the earthquake happened (green  
21 circles, left).

22 All reported SSEs (i.e. three in Guerrero and two in Oaxaca) and the post-seismic slip of the Pinotepa  
23 earthquake overlap one another outlining a 650 km long, trench-parallel band of aseismic stress

1 release (Fig. 1). Effects of the earthquakes on the SSE activity or, inversely, of the SSEs on the  
2 earthquakes' initiation may have occurred due to static and/or dynamic stress/strain perturbations.  
3 In the following we examine these possibilities.

4

- 5 • **Stress Transfer and Seismicity**

6 Stress transfer to active faults has long been recognized as a preponderant factor in earthquake  
7 occurrence (26). Although fault failure depends on the absolute stress level, changes of the Coulomb  
8 Failure Stress (CFS) explain remarkably well rupture sequences and seismicity-rate variations. CFS  
9 changes smaller than 50 kPa (0.5 bar) are often spatially well correlated (above 65%) with triggered  
10 seismicity and significantly larger (one order of magnitude) than values required for triggering slow  
11 earthquakes in subduction zones (27).

12 The 1 cm slip contour of the 2017 Guerrero SSE stopped about 80 km from the Puebla-Morelos  
13 intraslab earthquake hypocenter (Fig. 2A). The CFS on the seismogenic fault (i.e. within a 20 km  
14 radius from the hypocenter) due to the plate-interface aseismic slip evolution (SSE + PIC) reveals a  
15 rise of 50 kPa (0.5 bar) around the earthquake hypocenter in the 40 days preceding the rupture (Fig.  
16 S3E, Methods). Albeit this increment is in the upper limit of the 0.1-0.5 bar earthquake triggering  
17 threshold commonly referred in the literature (26) and similar to the one believed to have triggered  
18 the Mw7.3 (2014) Papanaoa earthquake by a SSE in Guerrero (5), interestingly, it occurred in the  
19 last stage of the SSE, when the PIC near the rupture area experienced a recovery, certainly affected  
20 by the evolution of the neighboring SSE. As discussed latter, the strong shaking produced in the  
21 seismogenic fault by the great Tehuantepec earthquake 11 days earlier, could significantly reduce  
22 the intraslab frictional strength and thus assist the Mw7.1 Puebla-Morelos rupture initiation (28)  
23 driven by the CFS induced by the aseismic slip at the plate interface. To our knowledge, this is the

1 first evidence that an SSE could initiate a devastating intraslab rupture such as the Puebla-Morelos  
2 earthquake.

3 Five months later, the Mw7.2 Pinotepa thrust earthquake took place at the Cocos – North American  
4 plate boundary (Fig. 1) while the 2017 Oaxaca SSE was unfolding (Fig. 3A). The detailed aseismic  
5 slip and CFS evolution on the plate interface preceding the earthquake is shown in Fig. S4. Around  
6 the hypocentral region there is a clear rise of CFS reaching cumulative values close to 400 kPa (4  
7 bar) (Fig. 4A). During the five months following the Mw8.2 Tehuantepec rupture and within a radius  
8 of 20 km from the Pinotepa earthquake hypocenter, the CFS experienced a sustained growth of 200  
9 kPa (2 bar) due to the SSE development to the north (Fig. 4B). During the same period, GPS  
10 inversions show that the interplate slip rate, which always remained in a coupling regime (i.e.  
11 smaller than the plate convergence rate), decreased until the initiation of the earthquake (i.e. the PIC  
12 increased from 0.1-0.2 up to  $\sim 0.65$ ). To better elucidate the mechanical process leading to the  
13 Pinotepa earthquake nucleation, we carefully analyzed the seismicity in the hypocentral region  
14 during the year preceding the event using two complementary template matching techniques  
15 (Methods, Figs. S5 and S6). Figure 4C shows 21-days event counts with magnitude larger than 2.1  
16 and foci within a 30 km radius from the hypocenter. Our seismic catalog has 431% more detections  
17 (5,977 earthquakes) than those reported by the Servicio Sismológico Nacional (SSN) above the  
18 completeness magnitudes for the same period and hypocentral distance. One clear feature stands  
19 out: seismicity raised steadily after the Mw8.2 Tehuantepec event until the Mw7.2 Pinotepa  
20 earthquake, especially during the two previous months (up to  $\sim 50\%$  increase), when the Oaxaca  
21 SSE induced the largest CFS increment in the hypocentral region (see also Fig. S4F).

22 The increase in CFS, PIC and seismicity rate in the hypocentral region before the Pinotepa  
23 earthquake strongly suggests that the dominant mechanism that led to the onset of rupture

1 corresponds to an asperity model; i.e. a heterogeneous initial stress in the source region was loaded  
2 at a mesoscale by the development of the SSE to the north until an overloaded nucleation patch, the  
3 asperity (e.g. subducted seamount), overcame the plate interface strength. Notice the outstanding  
4 correlation between the CFS concentration and the location of the precursor seismicity next to the  
5 earthquake hypocenter (Fig. 4A). Despite the increasing coupling of the plate interface (and CFS)  
6 during the preparedness of the earthquake, seismicity also increased. This scenario disfavors the  
7 putative widespread idea of a SSE-induced aseismic slip acceleration around the nucleation patch,  
8 observed for other large earthquakes (1, 2), as the main triggering mechanism for this event. The  
9 small magnitude precursor seismicity reveals small-scale processes that escape to our GPS  
10 inversions. However, this activity can be explained by a cascading rupture of small, neighboring  
11 asperities loaded by the mesoscale effect of the SSE evolution north of the hypocenter.

12 In addition, except for the large post-seismic slip of the Pinotepa earthquake and the very east  
13 portion of the 2017 Oaxaca SSE (Figs. 5B and 5D), static CFS perturbations produced by the  
14 earthquake sequence seems not to have had major bearing on the SSE activity.

#### 16 • **Plate Interface Dynamic Perturbations**

17 Abrupt changes in the slow crustal deformation pattern after the Tehuantepec and Pinotepa  
18 earthquakes (Fig. 3) suggest an effect of both events on the interplate aseismic slip that cannot be  
19 explained by static stress transfers, as shown in the last section. However, dynamic stress or strain  
20 perturbations produced by seismic waves may have important implications in the elastic properties  
21 of fault zone materials (e.g., transient reduction of the bulk modulus) and the slip behavior,  
22 especially where slow earthquakes take place (6, 7, 9, 28-30). For instance, long-period surface

1 waves from the 2010 Mw8.8 Maule earthquake triggered deep tremor in Guerrero and likely  
2 reactivated an ongoing SSE (8).

3 We estimated dynamic perturbations at the plate interface for both earthquakes of the sequence  
4 (Methods). Figure 5A shows the CFS peak values produced by the Rayleigh waves of the Mw8.2  
5 Tehuantepec event (Fig. S7) beneath strong motion stations in south-central Mexico. Dynamic  
6 perturbations around the 2017 Oaxaca SSE region lasted about 80 s and are characterized by three  
7 major wave cycles with CFS values ranging between 75 and 200 kPa, and absolute dilations between  
8  $1.4 \times 10^{-6}$  and  $6.0 \times 10^{-6}$  (Fig. S8). Albeit the dynamic triggering of slow earthquakes also depends  
9 on the (uncertain) preexistent fault condition, dynamic dilations from the Tehuantepec event are two  
10 orders of magnitude larger than those produced in Japan by the great Sumatra-Andaman 2004  
11 earthquake, which triggered widespread tremor in Shikoku and Tokai regions (6) and CFSs about  
12 eight times larger (31). The earthquake triggered tremor in Oaxaca (23) and a SSE in the San  
13 Andreas fault (10), 3,000 km northwest from the source. Since the 2017 Oaxaca SSE initiated before  
14 the earthquake and considering that tremor sensitivity increases as the slow slip develops (32), it is  
15 plausible that such dynamic perturbations were responsible of the large SSE enhancement and thus  
16 of the sudden change of the crustal deformation pattern in the region (Fig. 3A).

17 Given that the Mw7.2 Pinotepa earthquake is a much smaller event that occurred closer to the  
18 (presumably) triggered 2018 Guerrero SSE (Figs. 2B and 3B), shorter-period body waves could also  
19 affect the SSE that was unfolding in Oaxaca at the moment of rupture. Figure 5C shows the  
20 complete-wavefield CFS maximum values simulated on the plate interface for the earthquake using  
21 the DGCrack numerical platform (33) (Methods, Fig. S9). Values range between 100 and 150 kPa  
22 within the 2018 Guerrero SSE slip area, and overcome 400 kPa in the post-seismic slip region  
23 downdip from the epicenter. In contrast, the co-seismic static CFS change produced by the

1 earthquake is at least two orders of magnitude smaller in the same SSE region (Fig. 5D). This  
2 indicates that seismic waves of the Pinotepa earthquake could also be responsible for triggering the  
3 second SSE in Guerrero and therefore the change in the regional deformation pattern at the time of  
4 the event (Fig. 3B).

#### 6 • **Mechanics of SSEs Dynamic Triggering**

7 To assess whether seismic waves from the Tehuantepec and Pinotepa earthquakes could explain the  
8 abrupt changes of the crustal deformation pattern, we conducted numerical simulations of SSEs in  
9 the framework of rate-and-state (R&S) friction models subject to the stress dynamic perturbations  
10 estimated for both earthquakes. Previous studies with similar methods (10, 34) focused on  
11 dynamically triggered SSEs when the perturbation occurs in the inter-SSE period. However, the  
12 Tehuantepec and Pinotepa earthquakes happened during a large SSE in Oaxaca (Fig. 3), making this  
13 a unique opportunity to understand the mechanics of SSEs when seismic waves from M7+ and  
14 larger regional earthquakes perturb them in a tectonic environment where both phenomena are  
15 frequent.

16 Following Wei et al. (34), we developed a 2D R&S SSE model for the Oaxaca region (Fig. 6A)  
17 (Methods, Fig. S10). Figure 6C shows the model response to dynamic stresses estimated for the  
18 Tehuantepec earthquake at the plate interface under station YOIG, which is located above the 2018  
19 Oaxaca SSE slip area (Figs. 5A and S8). Final slip due to the stress perturbation is about twice the  
20 value of the reference, spontaneous SSE (Fig. 6C). Figure 6B shows the “aseismic slip jump”  
21 induced by this perturbation, where the propagation speed of the SSE front experiences an abrupt  
22 acceleration which, in turn, implies a change of the same order in the surface displacements. The  
23 higher the CFS peak value, the larger are both the final slip and the SSE front and slip accelerations

1 (Fig. 6C). The same happens with the perturbations estimated for the Pinotepa earthquake (Fig. 6D).  
2 However, despite that peak values over the 2017 Oaxaca SSE region are significantly larger than  
3 those induced by Rayleigh waves from the Tehuantepec event ( $> 250$  kPa), they overcome the SSE  
4 triggering threshold for a much shorter time (intense phase durations for the Mw8.2 and Mw7.2  
5 events are  $\sim 75$  s and  $\sim 13$  s, respectively). Consequently, the slip increment associated with each  
6 wavelet exceeding the threshold is smaller. This is clear in the insets of Figures 6C and 6D, where  
7 the slip rate response and cumulative slip increment due to several waves from the Pinotepa  
8 earthquake is comparable to the increment of a single phase of the Tehuantepec event. Thus, the  
9 dominant period of seismic waves also controls its SSE triggering potential and thus the effective  
10 fault response (Fig. S10D). Since our model considers only along-dip SSEs propagation and the  
11 actual slip in Oaxaca and Guerrero migrated predominantly along-strike, it is clear that seismic  
12 waves from both earthquakes could produce a much longer SSE evolution than theoretically  
13 predicted by our simple model, explaining thus the observed crustal rebounds initiated with both  
14 ruptures (Fig. 3).

## 16 Discussion

17 During two years, between June 2017 and July 2019, in addition to the devastating earthquake  
18 sequence, five large SSEs ( $M_w > 6.9$ ) occurred in southcentral Mexico over a trench-parallel  
19 continuous band of 650 km in length with a cumulative moment magnitude Mw7.4 (Fig. 1, Table  
20 1). Three of them in Guerrero, and the other two in Oaxaca interspersed by the Pinotepa earthquake  
21 post-seismic slip with Mw7.2. Among all aseismic events, only the 2017 Guerrero and Oaxaca SSEs  
22 initiated before the earthquake sequence, so that 87% of the total aseismic moment was released  
23 during the 1.7 years following the great Mw8.2 Tehuantepec rupture, when the earthquake sequence

1 started. Although the three Guerrero SSEs nucleated in different regions (Fig. 2), all of them overlap  
2 downdip of the Northwest Guerrero seismic gap with a slip larger than 6 cm each (Figs. 1, 2 and  
3 S2). Unlike the last 20 years, during which all SSEs occurred every  $\sim 4$  years in Guerrero (six events  
4 between 1998 and 2017) (5), the last two events reported here had much smaller recurrence periods,  
5 of 0.25 and 0.5 years for the 2018 and 2019 SSEs, respectively. In Oaxaca something unusual also  
6 happened; the plate interface slipped (aseismically) continuously for the whole two years period  
7 with at least two reactivations, one during the post-seismic relaxation of the Mw7.2 Pinotepa  
8 earthquake, and the other one around November 2018, when the second Oaxaca SSE initiated.  
9 Similar M7+ thrust earthquakes had occurred in Oaxaca and Guerrero (5, 21), but none was followed  
10 by a SSE in the last stage of their post-seismic relaxation. All these observations strongly suggest  
11 that, in addition to the dynamic effect of the seismic waves from the Tehuantepec and Pinotepa  
12 earthquakes on the ongoing SSEs, the elastic and frictional properties of the plate interface across  
13 the entire Mexican subduction zone underwent a transient change due to the extremely large,  
14 unprecedented ground shaking on September 8, 2017.

15 When seismic waves exceed a certain strain threshold, fault gouge materials undergo abnormal non-  
16 linear changes that can bring them to a metastable state facilitating the triggering of earthquake and  
17 SSEs (28-30). Although no mechanical changes have yet been observed in the properties of the  
18 plate-interface fault-zone due to strong shaking, large seismic waves can affect the continental crust  
19 down to its root for several years (35). It is thus reasonable that the Mw8.2 Tehuantepec earthquake  
20 is responsible for the extraordinary disruption of the SSE cycle observed at the regional scale, and  
21 even for facilitating the dynamic triggering of the SSEs that we report here. The same hypothesis is  
22 valid for the Puebla-Morelos and Pinotepa earthquakes, triggered by the 2017 Guerrero and Oaxaca  
23 SSEs, respectively, where the loss of fault zone rigidity on both seismogenic faults could occur on

1 September 8 (2017) assisting their rupture initiation (28). Therefore, continuous monitoring of the  
2 regional deformation and seismic properties of the crust is essential to assess the possibility of future  
3 large earthquakes and thus to have a clearer picture of the temporal evolution of the seismic hazard  
4 in subduction zones.

5

6

## 1 **Methods**

### 2 • Elastostatic adjoint inversion

3 The method used to invert the GPS time series, ELADIN (ELastostatic ADjoint INversion) (25),  
4 simultaneously determines the distribution of coupling and SSEs in the plate interface to explain the  
5 surface displacements. To this purpose, the method solves a constrained optimization problem based  
6 on the adjoint elastostatic equations with Tikhonov regularization terms, a von Karman  
7 autocorrelation function and a Gradient Projection method to guarantee physically-consistent slip  
8 restrictions. The main parameters governing the inversions are the correlation length of the von  
9 Karman function,  $L$ , which controls the wavenumber content of the solution, and the precision  
10 matrix, which weights the data according to its confidence. We assumed a von Karman Hurst  
11 exponent of 0.75 and  $L = 40$  km. Comprehensive resolution tests show that, given the problem  
12 geometry (i.e. the 3D plate interface and the available stations, Fig. 1), these values maximize the  
13 restitution index for slip patches larger than  $\sim 80$  km length and minimize the data misfit error (25).

14 Although GPS data has been carefully processed to generate the displacement time series (see next  
15 section), there always remain trailing errors and physical signals that do not correspond to tectonic  
16 processes (Fig. S1). The precision matrix allows to minimize the effect of such noise in the inversion  
17 results and corresponds to the inverse of the data variance per station and time window. To do this,  
18 especially in the vertical component, numerous synthetic and real data inversions lead us to adjust  
19 the precision matrix (i.e., the data weights) to ensure that polarities of the vertical-displacement are  
20 well explained by the inverted models, while maintaining the best horizontal-displacement fits (25).

21 The data variance for each component and time window is computed from the differences between  
22 daily displacement values and a moving, locally weighted LOESS function (i.e. 2nd order  
23 polynomial regressions with a half-window time support).

1 For the inversions we removed the coseismic displacements produced by the three large earthquakes  
 2 and improved the 3D plate interface geometry introduced by Radiguet et al. (5) based on the work  
 3 of Ferrari et al. (36), which compiles relocated seismicity, receiver functions and tomography  
 4 studies in southern Mexico. We refined the final geometry beneath Oaxaca based on recent  
 5 magneto-telluric and receiver function analysis (37, 38) (Fig. 1) and assumed a suitable 1D four-  
 6 layer regional structure (39). The slip vector is decomposed in the plate-convergence (pc) and pc-  
 7 perpendicular directions, which vary along the plate interface (40). Restrictions were imposed to  
 8 meet reasonable plate coupling constraints (i.e. backslip smaller than the cumulative plate motion  
 9 in the associated time window) and moderate pc-perpendicular slip by means of an iterative Gradient  
 10 Projection method (25), so that the slip rake could only vary 30 degrees with respect to the plate  
 11 convergence direction.

12  
 13 • GPS data processing

14 We used continuous records in 57 permanent GPS stations spread across central Mexico (Fig. 1).  
 15 The stations belong to three different networks: the Mexico-Japan SATREPS-UNAM project (24),  
 16 the National Seismological Service (SSN-UNAM) and Tlalocnet (41). GPS data was processed  
 17 using two different methods: Gipsy 6.4 (42) and Gamit/Globk 10.7 (43). For the period between  
 18 October 23 (2016) to November 22 (2018), after carefully comparing both displacement timeseries  
 19 in all stations, we selected those with better signal to noise ratio and consistency with nearby stations  
 20 (Fig. S1A). For the period from November 22 (2018) to October 8 (2019), we only considered  
 21 selected timeseries calculated using Gipsy 6.4 (Fig. S1B).

22 The GIPSY displacement timeseries are estimated with a Precise Point Positioning strategy. The  
 23 station positions are defined in the International Terrestrial Reference Frame, year 2014 (ITRF

1 2014). For daily processing we used the Jet Propulsion Laboratory final and non-fiducial products  
2 (orbits and clocks). We generated observables using 2 model categories: (1) Earth models and (2)  
3 observation models. The Earth models include tidal effects (i.e. solid tides, ocean loading and tide  
4 created by polar motion), Earth rotation (UT1), polar motion, nutation and precession. Observation  
5 models, on the other hand, are related with phase center offsets, tropospheric effects and timing  
6 errors (i.e. relativistic effects). The troposphere delay is estimated like as random walk process. This  
7 effect is broken into wet and dry components. The azimuthal gradient and the dry component are  
8 estimated using GPT2 model and mapping function (TGIPSY1). The antennas phase center  
9 variations are considered through antenna calibration files. For receiver antennas, the correction is  
10 estimated taking the International GNSS Service (IGS) Antex file. We also applied a wide-lane  
11 phase bias to account for the ambiguity resolution and removed outliers.

12 The GAMIT displacement timeseries are estimated using a double difference method that calculates  
13 the between-station and satellites differences. It reduces satellite clock and orbit errors, localized  
14 atmospheric errors and cancels the effects of variations in the receiver clocks. The software  
15 incorporates final IGS (International GNSS Service) combination solutions for orbits (with  
16 accuracies of 1-2 cm) and Earth Orientation Parameters (EOP). Ionospheric and atmospheric  
17 corrections were applied during processing. Hydrostatic and water vapor delay are corrected using  
18 Vienna Mapping Functions (VMF). Solid Earth tide model (IERS03), ocean tidal loading  
19 (FES2004), tables for earth rotation values (nutation IAU2000, polar motion, universal time) and  
20 precession constant IAU76 are applied. The resulting GPS time series are calculated in the ITRF  
21 2014 reference frame and then rotated with respect to the fixed North American plate using the  
22 rotation pole. Post-processing of daily position time series includes offset corrections and outlier

1 removal that was performed with the help of python-based PYACS package developed by J.-M.  
2 Nocquet.

3  
4 • Template-matching seismicity analysis

5 To detect unreported seismicity within the Mw7.2 Pinotepa earthquake hypocentral region previous  
6 to the event, we applied two independent and complementary template matching (TM) techniques.  
7 In both cases, the waveform templates were earthquakes reported by the SSN with foci within 30  
8 km from the Pinotepa earthquake hypocenter (Lat: 16.218°, Lon: -98.014°, 16 km depth). We used  
9 continuous velocity records in three broadband stations with epicentral distance smaller than 115  
10 km during a one-year period preceding the earthquake, from March 1, 2017, to February 16, 2018  
11 23:39 (UTC time of the Mw7.2 earthquake).

12 The first technique (44) considers three permanent stations (PNIG, YOIG, TXIG) from the SSN  
13 network located in the state of Oaxaca (Fig. S5A). We used a set of 394 events (templates) reported  
14 in the SSN catalog and applied a bandpass Butterworth filter with corner frequencies of 1-8 Hz to  
15 reduce the noise, and to remove undesired regional and teleseismic events. For each template, we  
16 selected a cross-correlation window starting 1 seconds before the arrival of the S-wave and ending  
17 5 seconds after, only one detection is allowed every 25 seconds to avoid duplicates of the same  
18 event. A detection was confirmed when the stacked correlation coefficient (scc) in the three stations  
19 (nine channels) was larger than 0.41 and the median average deviation larger than 25 (Fig. S5C).  
20 To this end we performed a grid search in a plane of 4.5 km x 4.5 km around each template location  
21 (Fig. S5A) and looked for the maximum scc value. For preventing detectability variations, we only  
22 processed those days with data for all components in the three stations.

1 The second technique considers only the waveforms on the three channels of the station PNIG, the  
2 closest site to the earthquake epicenter (21 km, Fig. S5B). For generating the templates, we selected  
3 4,105 events from the catalog reported by the SSN in the period between March 1, 2017 and March  
4 31, 2018. The waveforms were cut 0.2 seconds before the P-phase arrival and 0.5 seconds after the  
5 S-phase arrival, and filtered using a zero-phase Butterworth bandpass filter with corner frequencies  
6 at 3 Hz and 12 Hz. The template matching was performed using the Python package EQcorrscan  
7 (45) and the detection threshold was set to 0.9 of the average cross-correlation value in the three  
8 channels. Single-station detections have proved to be a powerful tool to find earthquakes that are  
9 small and located close to certain stations, but that get too attenuated to be detected at farther stations  
10 given high cross-correlation thresholds (46). Furthermore, a visual inspection of hundreds of  
11 waveforms helped us verify that the timing and the relative amplitudes of the ballistic P and S waves  
12 in the three components are very similar to the parent templates, guaranteeing that the detected  
13 signals are, indeed, earthquakes that share a common hypocentral location as the template events  
14 (Fig. S5D). For this second matched filter technique we allow inter-event times to be greater or  
15 equal to 10 seconds, keeping only the best correlated detections.

16 To assign a common magnitude to all detections,  $M_L$ , we determined an attenuation relationship  
17 specific to PNIG using the LocMagInv code (46) (Fig. S6A). Instead of inverting for the magnitudes,  
18 we used the cataloged magnitudes from the SSN for events with SNR greater or equal to 5 and  
19 inverted only for the geometric spread, attenuation and station correction parameters from horizontal  
20 displacement records (mm) (i.e. arithmetic mean). To obtain the displacements, we integrated  
21 velocity records in the bandwidth 3-12 Hz. We only used the available horizontal components for  
22 each event.

1 We detected 3,156 events with the first technique (Fig. S5A) and 5,064 with the second (Fig. S5B),  
2 which represent a 180% and 350% detection increase, respectively, as compared with the 1,125  
3 earthquakes reported by the SSN in the same period and within a 30 km hypocentral radius.  
4 Detections from both techniques were integrated into a single catalog avoiding duplicate events  
5 (Fig. 4D). Figure S6C shows the frequency-magnitude histograms for both, our TM detections and  
6 the SSN catalog, where the cutoff completeness  $M_L$  magnitudes correspond to 2.1, 2.4 and 3.2, for  
7 local detections (method two), regional detections (method one) and the SSE catalog, respectively.  
8 Since TM method one uses nine seismic channels (i.e. the three components of three stations) at a  
9 regional scale, its detections very likely correspond to events with hypocentral locations close to  
10 those of the templates that lie, all of them, within 30 km from the Pinotepa earthquake hypocenter.  
11 Thus, we used these detections for relatively large events to check how well method two, which  
12 only considers local records at PNIG (i.e. the three component), detected earthquakes within such  
13 hypocentral vicinity. Figure S6D show a Venn diagram for all catalogs where we see that 72% of  
14 regional detections were also found using only local records.

15  
16 • Dynamic Perturbations at the Plate Interface

17 From Strong Motion Records: For the Mw8.2 Tehuantepec event we used radial and vertical  
18 displacement records at 25 s period from strong motion stations in south-central Mexico (Figs. 5A  
19 and S7C) to estimate the strain field produced by the Rayleigh waves fundamental mode at depth,  
20 and then the associated CFS (apparent friction coefficient of 0.5) over the 3D plate interface in the  
21 plate-convergence slip direction (Fig. S8A). Values in Fig. 5A at sites without interface below  
22 correspond to a horizontal surface at 50 km depth.

1 To estimate the surface-wave dynamic deformations (and tractions) at depth from observed ground  
2 displacements (i.e. double integration of single-station strong motion records) we followed a two-  
3 fold procedure: First, we estimated the displacement at depth (i.e. at the plate interface below each  
4 site, Fig. 5A) by modulating the field with the associated surface waves eigenfunctions for the  
5 chosen period within a four-layer regional model determined from the dispersion of surface waves  
6 (39) (Fig. S7D). Then, to estimate the whole strain tensor, we computed the horizontal deformations  
7 assuming a phase velocity of 3.5 km/s (31), and the vertical deformations by deriving the  
8 eigenfunctions in that direction. Although Love waves can also have SSE triggering potential, in  
9 the analysis we only considered perturbations from Rayleigh waves. Figure S8 shows, for the  
10 Mw8.2 Tehuantepec earthquake, the traction vector and CFS time series on the 3D plate interface  
11 along the plate-convergence slip-rate direction and dilation time series below some selected sites.

12 To validate our procedure, we compared estimated (with our method) synthetic tractions with the  
13 exact solution for the Lamb's problem (i.e. for the wavefield excited by a single vertical force on  
14 top of a homogenous halfspace) at depth over a horizontal plane (Figs. S7A and S7B). The elastic  
15 properties of the medium are  $\alpha = 5.6$  km/s,  $\beta = 3.233$  km/s,  $\rho = 2700$  kg/m<sup>3</sup>, the surface station lies  
16 300 km away from the source and the buried point is 20 km below the station. In this example,  
17 tractions were estimated for 10 s period. However similar, satisfactory results were obtained for  
18 different periods and depths.

19 From 3D Numerical Simulations: To estimate the Mw7.2 Pinotepa earthquake (complete-wavefield)  
20 dynamic perturbations at the plate interface we performed a 3D kinematic-source numerical  
21 simulation by means of an hp-adaptive discontinuous Galerkin finite-element method (DGCrack)  
22 (33). The domain is discretized with a non-structured tetrahedral mesh considering a 3D crustal  
23 velocity model of the Guerrero-Oaxaca subduction zone (47) that incorporates the real topography

1 and bathymetry, as well as the geometry of the plate interface (Fig. S9A). The mesh size is 900 x  
2 380 x 104 km in the along-trench, trench-perpendicular and vertical directions, respectively, with  
3 approximately 11 million elements to achieve a numerical accuracy up to 1 Hz. We run DGCrack  
4 in 512 cores on the UNAM supercomputer platform Miztli to complete 260 seconds of numerical  
5 simulation spending 12.5 hours of total computer elapsed time. To simulate the finite source, we  
6 first used the low-wavenumber slip solution of the Pinotepa earthquake estimated by the USGS (Fig.  
7 S9B-up). Then, we discretized this solution into subfaults of 1 x 1 km and add high-wavenumber  
8 slip perturbations that are stochastically generated using a von Karman power spectral density (PSD)  
9 function to enhance the radiation of high frequencies following the methodology of Pulido et al.  
10 (48) (Fig. S9B-down). The slip-rate of every subfault follows a regularized Yoffe function and the  
11 rupture evolution is described by the spatial distribution of the slip, rise time, rupture velocity and  
12 peak time (i.e., the time to reach the peak slip-rate in every subfault) (Fig. S9C). These kinematic  
13 source parameters are heterogeneously distributed by means of a pseudo-dynamic rupture generator  
14 that considers the 1-point and 2-point statistics of each source parameter as well as their spatial  
15 interdependency extracted from dynamic rupture simulations. We validate the earthquake  
16 simulation by comparing the horizontal geometric mean of the observed and synthetic peak ground  
17 velocities (PGV) in different hard-site strong motion stations (Fig. S9D).

18 Since the resolution of the GPS time series does not allow distinguishing whether the Tehuantepec  
19 or Puebla-Morelos earthquakes (only eleven days in between them) produced the abrupt change of  
20 the crustal deformation pattern observed in Fig. 3A, we also estimated the dynamic perturbations  
21 on the plate interface due to the intraslab, normal-faulting, Mw7.1 Puebla-Morelos event using the  
22 same numerical procedure but taking a finite-source solution determined from the inversion of  
23 strong motions (17). Results are shown in Fig. S3F, where we appreciate that CFS peak values in

1 the 2017 Oaxaca SSE region (apparent friction coefficient of 0.5) are smaller than those induced by  
2 the Tehuantepec earthquake (Fig. 5A) (i.e.  $< 60$  kPa). Considering also that the duration of intense  
3 shaking by the Mw7.1 is much shorter than that produced by the Mw8.2 Tehuantepec event (i.e. its  
4 SSE triggering potential is lower, Fig. S10D) and that tremor activity in Oaxaca highly increased a  
5 few hours after the Tehuantepec earthquake (23), then we conclude that triggering of the 2017  
6 Oaxaca SSE was produced by seismic waves from the Mw8.2 event.

7  
8 • Rate and State Friction SSE Model

9 Assuming a 6 cm/yr plate convergence (40), we developed a R&S fault reference model for the  
10 Oaxaca region that spontaneously generates SSEs every 1.5 years with maximum slip of  $\sim 10$  cm  
11 (Fig. S10C), which is a reasonable approximation of the SSE activity in that province (21). The  
12 model assumes a planar fault dipping 13 degrees in a 2D elastic half-space (Figs. 6A and S10A).  
13 Following Wei et al. (34) and based on the SSEs slip distributions (Figs. 2C and 3A), the model is  
14 consisted of a velocity-weakening (VW) fault segment between 20 and 45 km depth where SSEs  
15 take place encompassed by stable, velocity-strengthening (VS) layers (Fig. S10B). Uniform,  
16 dynamic stress perturbations from the 2017 Mw8.2 Tehuantepec earthquake and the 2018 Mw7.2  
17 Pinotepa earthquake were inputted around the middle stage of a spontaneously initiated SSE at all  
18 depth with different scaling factors (Fig. 6) to consider the variations and uncertainties of both, the  
19 reference model and the CFS estimates throughout the SSE region.

20

1 **References:**

- 2 1. A. Kato *et al.*, Propagation of slow slip leading up to the 2011 M(w) 9.0 Tohoku-Oki  
3 earthquake. *Science* **335**, 705-708 (2012).
- 4 2. S. Ruiz *et al.*, Intense foreshocks and a slow slip event preceded the 2014 Iquique Mw 8.1  
5 earthquake. *Science* **345**, 1165-1169 (2014).
- 6 3. K. Obara, A. Kato, Connecting slow earthquakes to huge earthquakes. *Science* **353**, 253-257  
7 (2016).
- 8 4. N. Uchida, T. Inuma, R. M. Nadeau, R. Bürgmann, R. Hino, Periodic slow slip triggers  
9 megathrust zone earthquakes in northeastern Japan. *Science* **351**, 488-492 (2016).
- 10 5. M. Radiguet *et al.*, Triggering of the 2014 Mw7.3 Papanoa earthquake by a slow slip event in  
11 Guerrero, Mexico. *Nature Geoscience* **9**, 829-833 (2016).
- 12 6. M. Miyazawa, J. Mori, Evidence suggesting fluid flow beneath Japan due to periodic seismic  
13 triggering from the 2004 Sumatra-Andaman earthquake. *Geophys. Res. Lett.* **33**, (2006).
- 14 7. J. L. Rubinstein *et al.*, Seismic wave triggering of nonvolcanic tremor, episodic tremor and slip,  
15 and earthquakes on Vancouver Island. *J. Geophys. Res.* **114**, (2009).
- 16 8. D. Zigone *et al.*, Triggering of tremors and slow slip event in Guerrero, Mexico, by the 2010  
17 Mw 8.8 Maule, Chile, earthquake. *Journal of Geophysical Research: Solid Earth* **117**, B09304  
18 (2012).
- 19 9. L. M. Wallace *et al.*, Large-scale dynamic triggering of shallow slow slip enhanced by  
20 overlying sedimentary wedge. *Nature Geoscience* **10**, 765-770 (2017).
- 21 10. E. Tymofyeyeva *et al.*, Slow Slip Event On the Southern San Andreas Fault Triggered by the  
22 2017 Mw8.2 Chiapas (Mexico) Earthquake. *Journal of Geophysical Research: Solid Earth* **124**,  
23 9956-9975 (2019).

- 1 11. P. Audet, Y. Kim, Teleseismic constraints on the geological environment of deep episodic slow  
2 earthquakes in subduction zone forearcs: A review. *Tectonophysics* **670**, 1-15 (2016).
- 3 12. V. M. Cruz-Atienza, C. Villafuerte, H. S. Bhat, Rapid tremor migration and pore-pressure  
4 waves in subduction zones. *Nat Commun* **9**, 2900 (2018).
- 5 13. E. Warren-Smith *et al.*, Episodic stress and fluid pressure cycling in subducting oceanic crust  
6 during slow slip. *Nature Geoscience* **12**, 475-481 (2019).
- 7 14. D. Melgar *et al.*, Deep embrittlement and complete rupture of the lithosphere during the Mw 8.2  
8 Tehuantepec earthquake. *Nature Geoscience* **11**, 955-960 (2018).
- 9 15. G. Suárez *et al.*, Large scale lithospheric detachment of the downgoing Cocos plate: The 8  
10 September 2017 earthquake (Mw 8.2). *Earth Planet Sc Lett* **509**, 9-14 (2019).
- 11 16. S. K. Singh *et al.*, Deadly Intraslab Mexico Earthquake of 19 September 2017 (Mw 7.1):  
12 Ground Motion and Damage Pattern in Mexico City. *Seismological Research Letters* **89**, 2193-  
13 2203 (2018).
- 14 17. A. Mirwald *et al.*, The 19 September 2017 (Mw7.1) Intermediate-Depth Mexican Earthquake:  
15 A Slow and Energetically Inefficient Deadly Shock. *Geophys Res Lett* **46**, 2054-2064 (2019).
- 16 18. V. Kostoglodov *et al.*, A large silent earthquake in the Guerrero seismic gap, Mexico. *Geophys*  
17 *Res Lett* **30**, (2003).
- 18 19. M. Radiguet *et al.*, Slow slip events and strain accumulation in the Guerrero gap, Mexico. *J.*  
19 *Geophys. Res.* **117**, B04305 (2012).
- 20 20. C. Villafuerte, V. M. Cruz-Atienza, Insights into the Causal Relationship between Slow Slip  
21 and Tectonic Tremor in Guerrero, Mexico. *J Geophys Res* **122**, (2017).
- 22 21. S. Graham *et al.*, Slow Slip History for the MEXICO Subduction Zone: 2005 Through 2011.  
23 *Pure and Applied Geophysics* **173**, 3445-3465 (2016).

- 1 22. J. Maury, S. Ide, V. M. Cruz-Atienza, V. Kostoglodov, Spatiotemporal Variations in Slow  
2 Earthquakes Along the Mexican Subduction Zone. *Journal of Geophysical Research: Solid*  
3 *Earth* **123**, 1559-1575 (2018).
- 4 23. A. Husker *et al.*, Characteristic Tectonic Tremor Activity Observed Over Multiple Slow Slip  
5 Cycles in the Mexican Subduction Zone. *Journal of Geophysical Research: Solid Earth* **124**,  
6 599-608 (2019).
- 7 24. V. M. Cruz-Atienza *et al.*, A Seismogeodetic Amphibious Network in the Guerrero Seismic  
8 Gap, Mexico. *Seismological Research Letters* **89**, 1435-1449 (2018).
- 9 25. J. Tago *et al.*, Adjoint Slip Inversion under a Constrained Optimization Framework: Revisiting  
10 the 2006 Guerrero Slow Slip Event. *Earth and Space Science Open Archive*, (2020).
- 11 26. R. S. Stein, The role of stress transfer in earthquake occurrence. *Nature* **402**, 605-609 (1999).
- 12 27. R. Nakata, N. Suda, H. Tsuruoka, Non-volcanic tremor resulting from the combined effect of  
13 Earth tides and slow slip events. *Nature Geoscience* **1**, 676-678 (2008).
- 14 28. P. A. Johnson, X. Jia, Nonlinear dynamics, granular media and dynamic earthquake triggering.  
15 *Nature* **437**, 871-874 (2005).
- 16 29. P. A. Johnson *et al.*, Nonlinear dynamical triggering of slow slip on simulated earthquake faults  
17 with implications to Earth. *Journal of Geophysical Research: Solid Earth* **117**, (2012).
- 18 30. A. A. Delorey, K. Chao, K. Obara, P. A. Johnson, Cascading elastic perturbation in Japan due  
19 to the 2012 Mw8.6 Indian Ocean earthquake. *Science Advances* **1**, e1500468 (2015).
- 20 31. M. Miyazawa, E. E. Brodsky, Deep low-frequency tremor that correlates with passing surface  
21 waves. *J. Geophys. Res.* **113**, (2008).
- 22 32. H. Houston, Low friction and fault weakening revealed by rising sensitivity of tremor to tidal  
23 stress. *Nature Geosci* **8**, 409-415 (2015).

- 1 33. J. Tago, V. M. Cruz-Atienza, J. Virieux, V. Etienne, F. J. Sánchez-Sesma, A 3D hp-adaptive  
2 discontinuous Galerkin method for modeling earthquake dynamics. *Journal of Geophysical*  
3 *Research: Solid Earth* **117**, (2012).
- 4 34. M. Wei, Y. Kaneko, P. Shi, Y. Liu, Numerical Modeling of Dynamically Triggered Shallow  
5 Slow Slip Events in New Zealand by the 2016 Mw 7.8 Kaikoura Earthquake. *Geophys Res Lett*  
6 **45**, 4764-4772 (2018).
- 7 35. Q.-Y. Wang *et al.*, Evidence of Changes of Seismic Properties in the Entire Crust Beneath Japan  
8 After the Mw 9.0, 2011 Tohoku-oki Earthquake. *Journal of Geophysical Research: Solid Earth*  
9 **124**, 8924-8941 (2019).
- 10 36. L. Ferrari, T. Orozco-Esquivel, V. Manea, M. Manea, The dynamic history of the Trans-  
11 Mexican Volcanic Belt and the Mexico subduction zone. *Tectonophysics* **522**, 122-149 (2012).
- 12 37. J. A. Arzate-Flores, R. Molina-Garza, F. Corbo-Camargo, V. Márquez-Ramírez, Low Angle  
13 Contact Between the Oaxaca and Juárez Terranes Deduced From Magnetotelluric Data. *Pure*  
14 *and Applied Geophysics* **173**, 3357-3371 (2016).
- 15 38. M. Rodríguez-Domínguez, X. Pérez-Campos, C. Montealegre-Cázares, R. W. Clayton, E.  
16 Cabral-Cano, Crustal structure variations in south-central Mexico from receiver functions.  
17 *Geophys J Int* **219**, 2174-2186 (2019).
- 18 39. M. Campillo, S. K. Singh, N. Shapiro, J. Pacheco, R. B. Hermann, Crustal structure south of  
19 the Mexican volcanic belt, base on group velocity dispersion. *Geofis Int* **35**, 361-370 (1996).
- 20 40. C. DeMets, R. G. Gordon, D. F. Argus, Geologically current plate motions. *Geophys J Int* **181**,  
21 1-80 (2010).

- 1 41. E. Cabral-Cano *et al.*, TLALOCNet: A Continuous GPS-Met Backbone in Mexico for  
2 Seismotectonic and Atmospheric Research. *Seismological Research Letters* **89**, 373-381  
3 (2018).
- 4 42. K. Lagler, M. Schindelegger, J. Böhm, H. Krásná, T. Nilsson, GPT2: Empirical slant delay  
5 model for radio space geodetic techniques. *Geophys Res Lett* **40**, 1069-1073 (2013).
- 6 43. T. A. Herring, R. W. King, M. A. Floyd, S. C. McClusky, GPS Analysis at MIT. *GAMIT*  
7 *Reference Manual*, (2018).
- 8 44. M. Liu, H. Li, M. Zhang, T. Wang, Graphics Processing Unit-Based Match and Locate (GPU-  
9 M&L): An Improved Match and Locate Method and Its Application. *Seismological*  
10 *Research Letters* **91**, 1019-1029 (2020).
- 11 45. C. J. Chamberlain *et al.*, EQcorrscan: Repeating and Near-Repeating Earthquake Detection and  
12 Analysis in Python. *Seismological Research Letters* **89**, 173-181 (2017).
- 13 46. R. Garza-Giron, E. Brodsky, Z. Spica, M. Haney, Clog and Crack: Opening and Closing  
14 Behavior During a Sustained Explosive Eruption as recorded by its Hidden Earthquakes. *Earth*  
15 *and Space Science Open Archive*, (2020).
- 16 47. Z. Spica *et al.*, 3-D shear wave velocity model of Mexico and South US: bridging seismic  
17 networks with ambient noise cross-correlations (C1) and correlation of coda of correlations  
18 (C3). *Geophys J Int* **206**, 1795-1813 (2016).
- 19 48. N. Pulido *et al.*, Scenario Source Models and Strong Ground Motion for Future Mega-  
20 earthquakes: Application to Lima, Central Peru. *B Seismol Soc Am* **105**, 368-386 (2015).

## 1 Acknowledgments

2 We especially thank Yoshihiro Kaneko and Yajing Liu for fruitful discussions to set the R&S fault  
3 model, Mathilde Radiguet for discussions on the SSEs inversion, the Servicio Sismológico Nacional  
4 of UNAM for providing GPS, strong motion and broadband data, and the Instituto de Ingeniería of  
5 UNAM for providing strong motion data. SSE inversions and earthquake numerical simulations  
6 were performed in the Gaia and Miztli supercomputing platforms. **Funding:** This work was  
7 supported by UNAM-PAPIIT grants IN113814 and IG100617, UNAM-DGTIC grant LANCAD-  
8 312, JICA-JST SATREPS-UNAM grant 15543611, CONACyT grants 6471, 255308 and PN15-  
9 639, US NSF grant 1654416, AMEXCID-SRE and the Ministry of Civil Protection of the State of  
10 Guerrero, Mexico. **Author contributions:** V.M.C.-A. conceived and led the study, performed the  
11 GPS inversions, estimated the Mw8.2 dynamic CFSs and wrote the manuscript. J.T. developed the  
12 ELADIN inversion method for the study. C.V. estimated the static CFSs, performed the DGCrack  
13 simulations and developed processing and visualization tools. M.W. developed and analyzed the  
14 SSE R&S models. R.G.G. and L.A.D. performed and analyzed the template-matching seismicity  
15 detections. V.K. and T.N. contributed with the GPS data analysis. S.I.F., J.R. and E.K. processed  
16 the GPS data and maintained the SATREPS-UNAM GPS stations. M.A.S. participated in the single-  
17 station dynamic CFS validation. V.M.C.-A. and Y.I. are the PIs of the SATREPS-UNAM project.  
18 All authors reviewed and edited the manuscript. **Competing interests:** Authors declare no  
19 competing interests. **Data and materials availability:** GPS and strong motion data from SSN are  
20 subject to restriction policies while broadband data is open access (see [www.ssn.unam.mx](http://www.ssn.unam.mx)). Strong  
21 motion data from I. de I. UNAM are available upon request (see [www.uis.unam.mx](http://www.uis.unam.mx)). SATREPS-  
22 UNAM GPS data has restriction policies until March 2025. Methods and codes are available upon  
23 request.

1 **Supplementary Materials**

2 Fig. S1. GPS displacement data.

3 Fig. S2. Aseismic-slip depth distribution.

4 Fig. S3. Aseismic slip and CFS preceding the Mw7.1 Puebla-Morelos earthquake.

5 Fig. S4. Plate interface aseismic slip and CFS preceding the Mw7.2 Pinotepa earthquake.

6 Fig. S5. Template-matching seismic detections preceding the Mw7.2 Pinotepa earthquake.

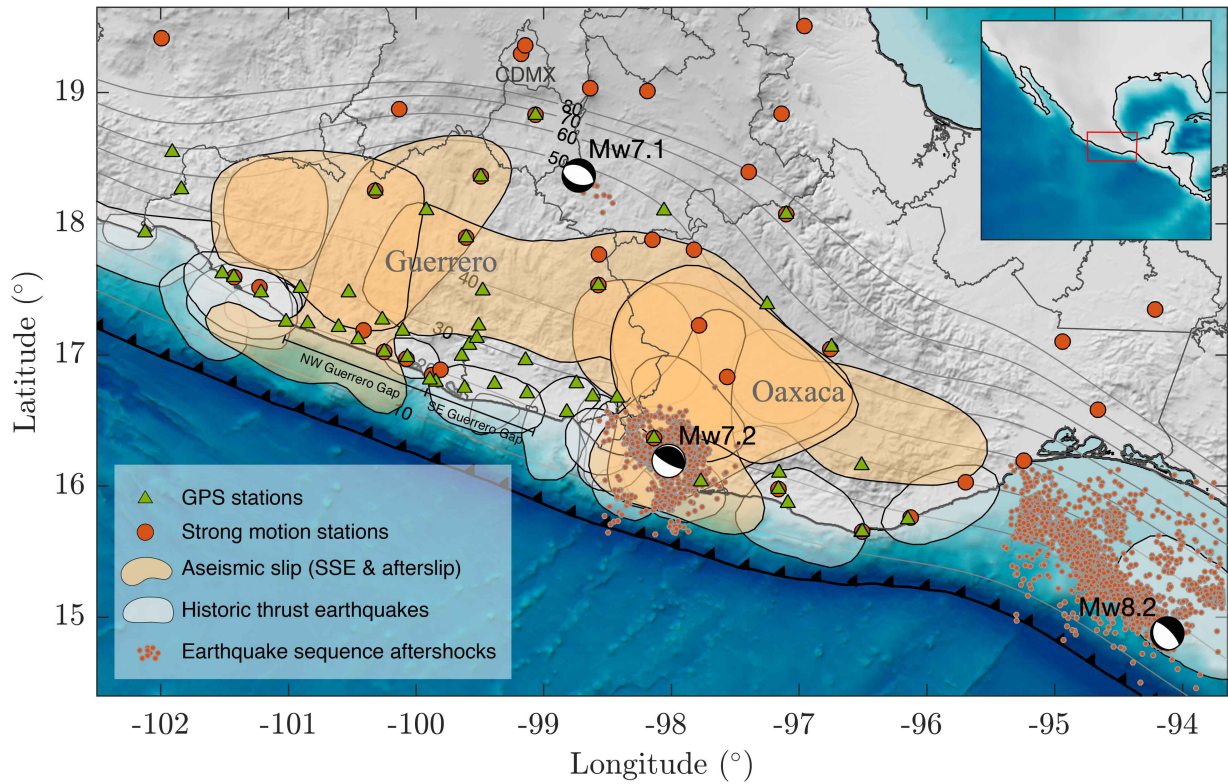
7 Fig. S6. Earthquake magnitude determination and seismicity analysis.

8 Fig. S7. Validation of the plate-interface dynamic perturbation estimates.

9 Fig. S8. Plate-interface dynamic perturbations for the Mw8.2 Tehuantepec earthquake.

10 Fig. S9. Discontinuous Galerkin 3D earthquake simulations.

11 Fig. S10. Rate-and-state friction model for the 2017 Oaxaca SSE.



1

2

3

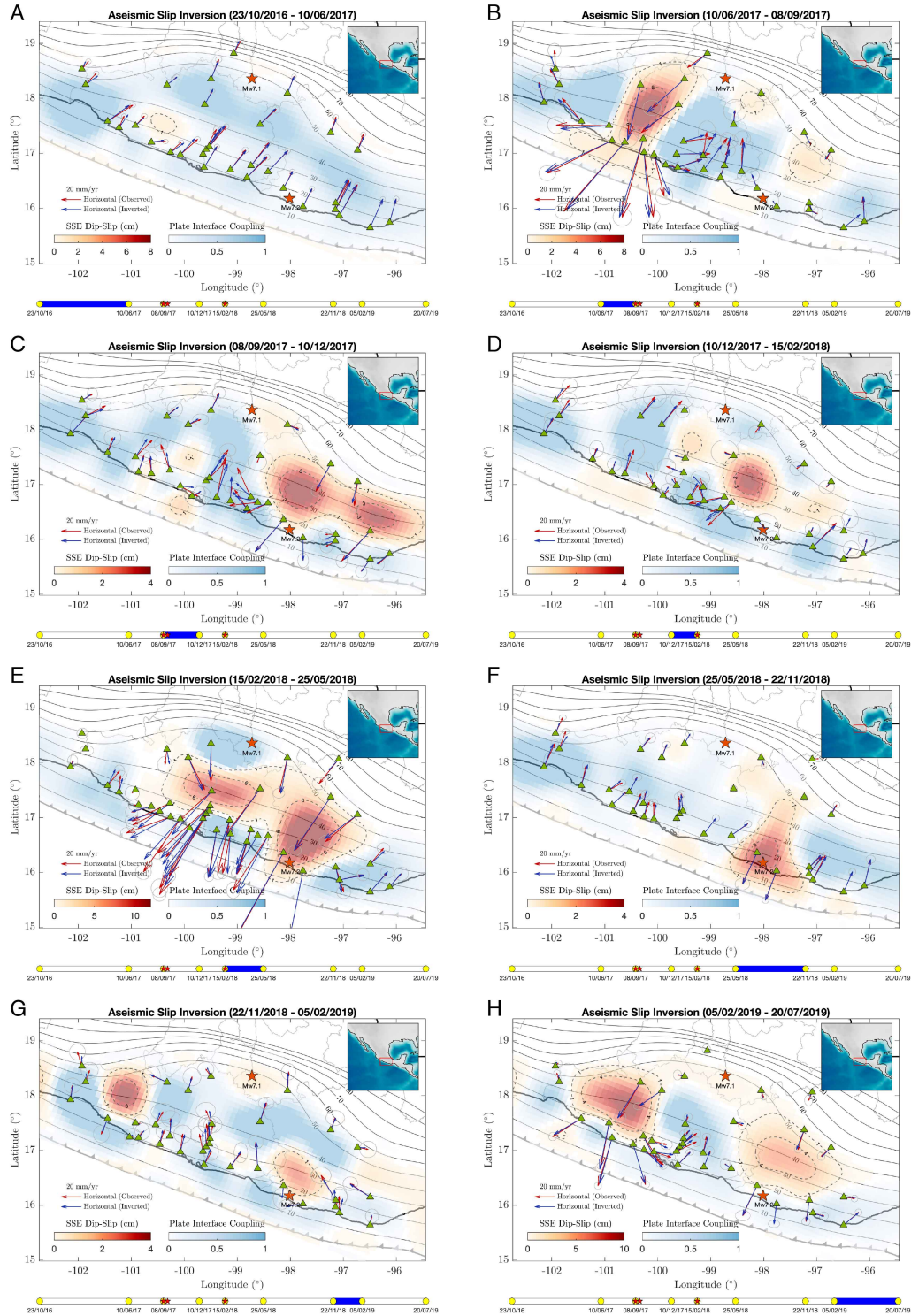
4

5

6

7

**Fig. 1.** Study region and instrumentation where the Tehuantepec (Mw8.2), Puebla-Morelos (Mw7.1) and Pinotepa (Mw7.2) earthquake sequence took place. Orange shaded areas depict the 1 cm aseismic slip contours imaged between June 2017 and July 2019 in the plate interface (gray contours). White shaded contours depict rupture areas of historic thrust earthquakes. Orange dots show the 10-days aftershock sequences as reported by the SSN except for the Mw7.1 earthquake, for which three-months aftershocks are reported.



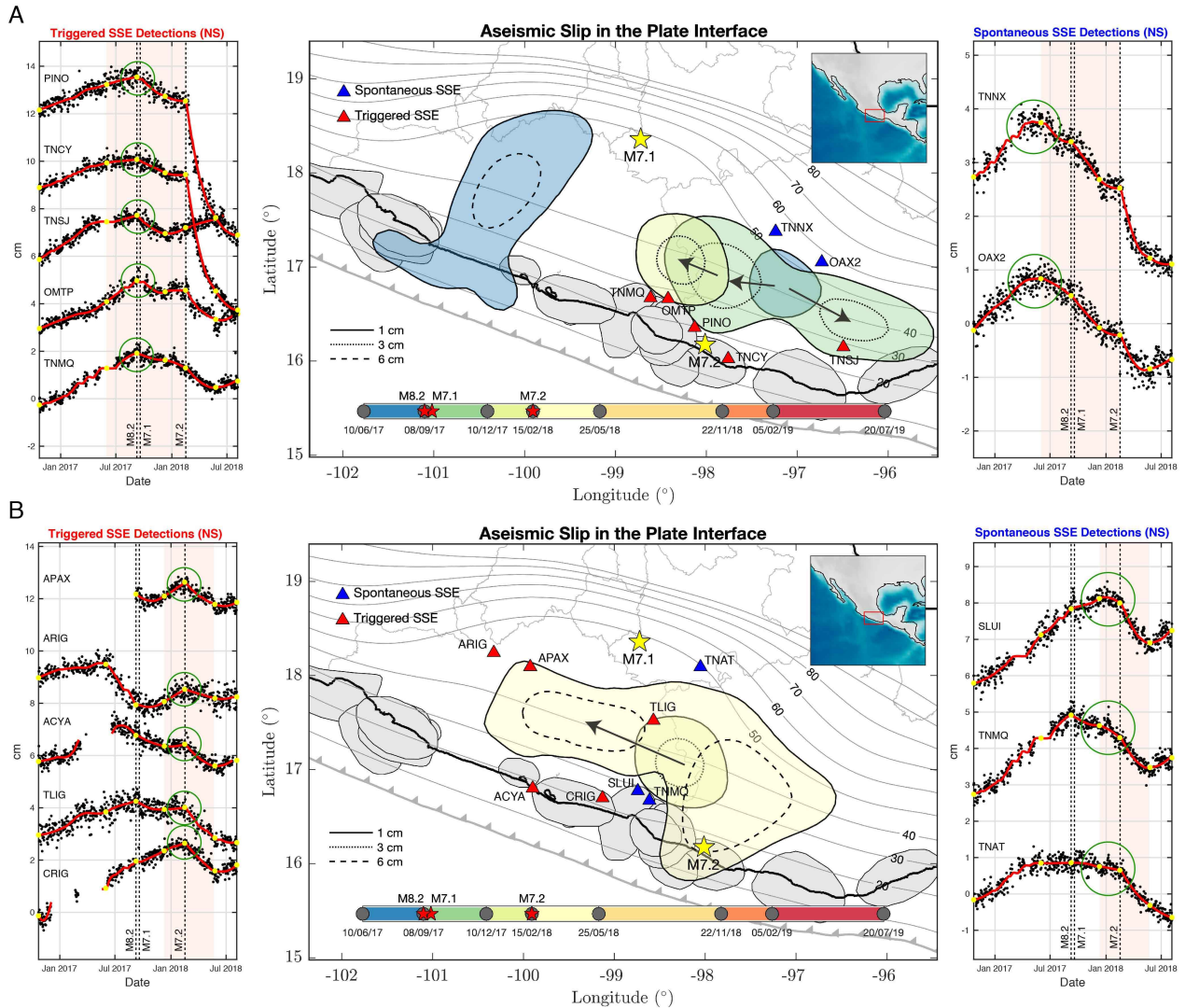
1

2

3

**Fig. 2.** Aseismic slip inversion results for the whole analyzed period across and after the earthquake sequence. Dashed slip contours are in centimeters. Yellow circles encompassing the

1 blue bar at the bottom of each panel indicate the dates of the associated inverted window, and  
2 red small stars, the Mw8.2 Tehuantepec, Mw7.1 Puebla-Morelos and Mw7.2 Pinotepa  
3 earthquakes timing, respectively, from left to right. Red and blue arrows show the observed and  
4 synthetic surface displacements, and the gray ellipses one standard deviation of the GPS data.



1

2

**Fig. 3.** Evolution of the aseismic (SSEs and post-slip) during the earthquake sequence. Pink shaded rectangles encompass the associated inverted windows for each panel (yellow dots). Blue triangles show GPS stations where spontaneously initiated or preexistent SSE are observed (right panels, green circles), while red triangles show the stations where triggered SSE are detected (left panels, green circles). Notice the abrupt reversal of the deformation pattern (from north to south) right when the Tehuantepec and Pinotepa earthquakes happened in the left panels (green circles).

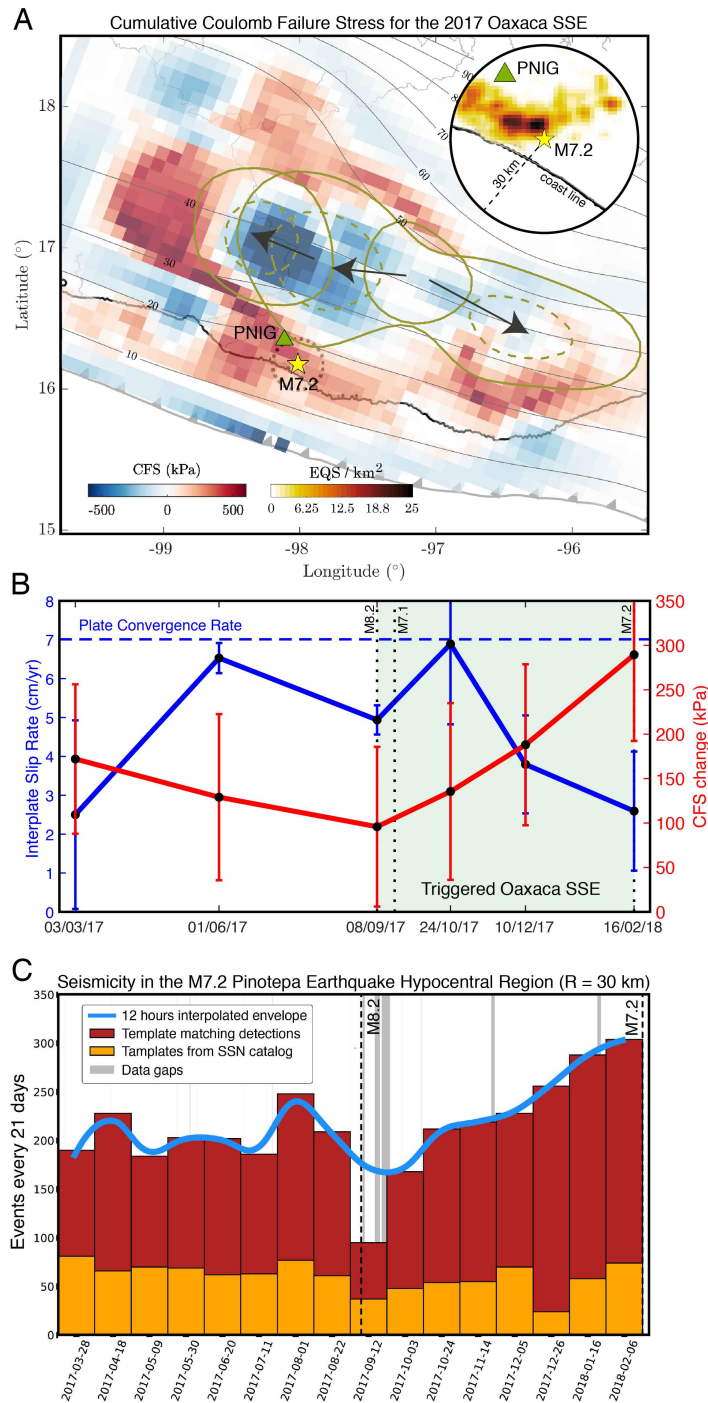
3

4

5

6

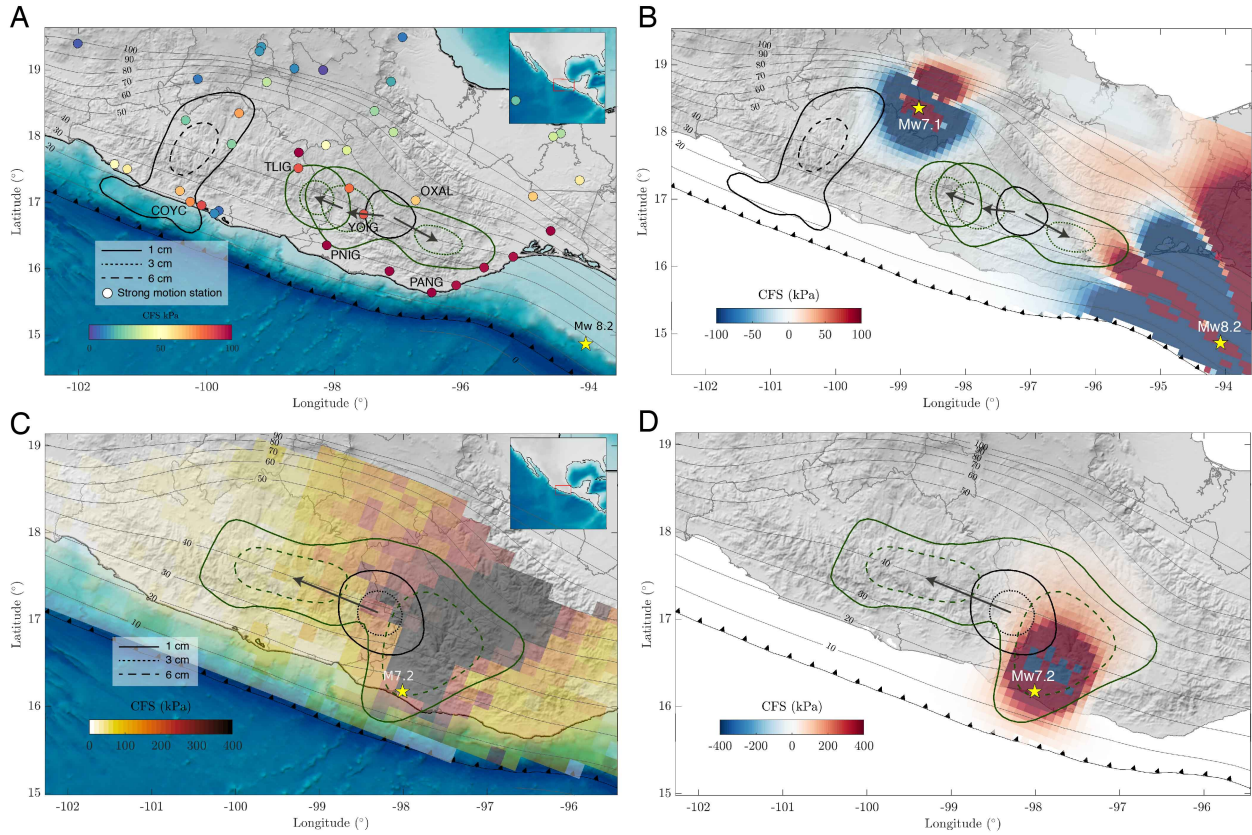
7



1

2 **Fig. 4.** CFS, PIC and seismicity rate evolution before the Pinotepa earthquakes nearby its  
 3 hypocenter. (A) 15-month cumulative CFS on the plate interface and spatial evolution of the 2017  
 4 Oaxaca SSE (1 cm slip solid contours and 3 cm slip dashed contours). Density of TM precursor

- 1 detections (inset). (B) Temporal evolution of the CFS change and the interplate slip rate within a 20
- 2 km radius from the Pinotepa earthquake hypocenter (dotted circle, panel A). See also Fig. S4. (C)
- 3 Seismicity rate evolution for  $M > 2.1$  events within 30 km from the Pinotepa earthquake hypocenter.



1

2

**Fig. 5.** Dynamic (peak values) and static CFSs on the 3D plate interface (gray contours) produced

3

by the Tehuantepec (A and B, respectively) and Pinotepa (C and D, respectively) earthquakes in the

4

plate convergence direction. Aseismic slip events right before the corresponding earthquake are

5

shown with black contours, while those occurred immediately after the earthquake are shown with

6

green contours. Dynamic stresses for the Tehuantepec event (A) where computed from actual strong

7

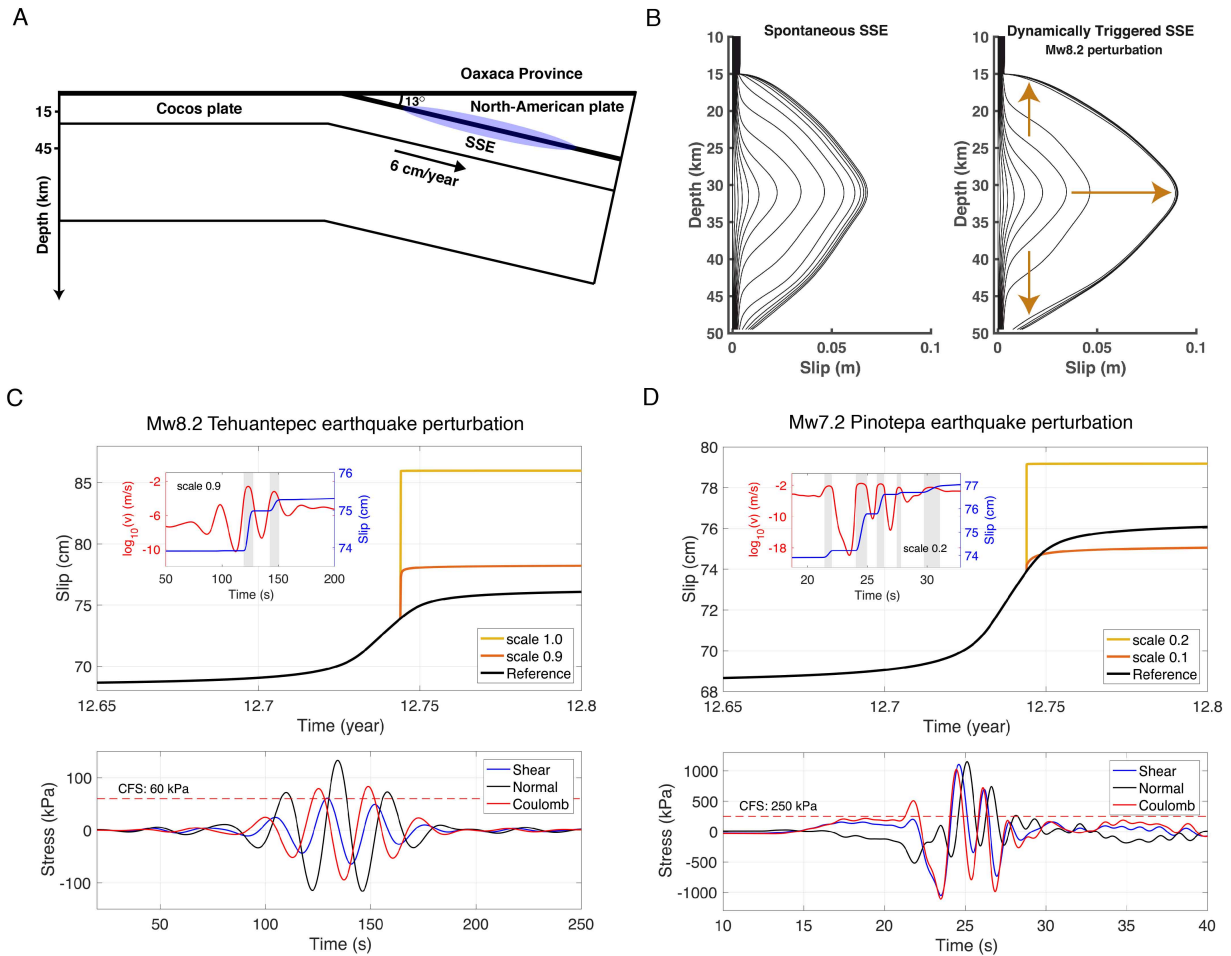
motion records at different sites (colored circles, see Fig. S8A). Estimates for the Pinotepa event

8

(C) where computed through a 3D finite-source numerical simulation of the earthquake (see Fig.

9

S9).



1  
2 **Fig. 6.** Rate-and-state fault model for SSE triggering by seismic-wave stress perturbations. (A)  
3 Synoptic 2-D model of the subduction zone in the study area. (B) Slip evolution of a spontaneous  
4 SSE and a dynamically triggered SSE in the rate-and-state friction model. The contours time  
5 increment is about 2 days. (C) Top, slip evolution of the SSE reference model and two triggered  
6 events at 31 km depth for stress perturbations due to the Mw8.2 Tehuantepec earthquake with  
7 different scaling factors. The inset shows the slip velocity and slip at that depth with 0.9 scaled  
8 perturbation. Bottom, stress perturbation used in these simulations. (D) Same as (C) but for the  
9 Mw7.2 Pinotepa earthquake. Please note that the scaling factors are different.

10

Guerrero			Oaxaca		
Aseismic Event	Date (dd/mm/yy)	Magnitude (Mw)	Aseismic Event	Date (dd/mm/yy)	Magnitude (Mw)
SSE	10/06/17 – 08/10/17	6.91	SSE	01/06/17 – 15/02/18	6.93
SSE	16/02/18 – 01/06/18	6.93	Pinotepa Post-slip	16/02/18 – 22/11/18	7.17
SSE	22/11/18 – 20/07/19	6.99	SSE	05/02/19 – 20/07/19	6.92

1 **Table 1.** Dates and moment magnitude (Mw) of all aseismic events reported in this work.

# Figures

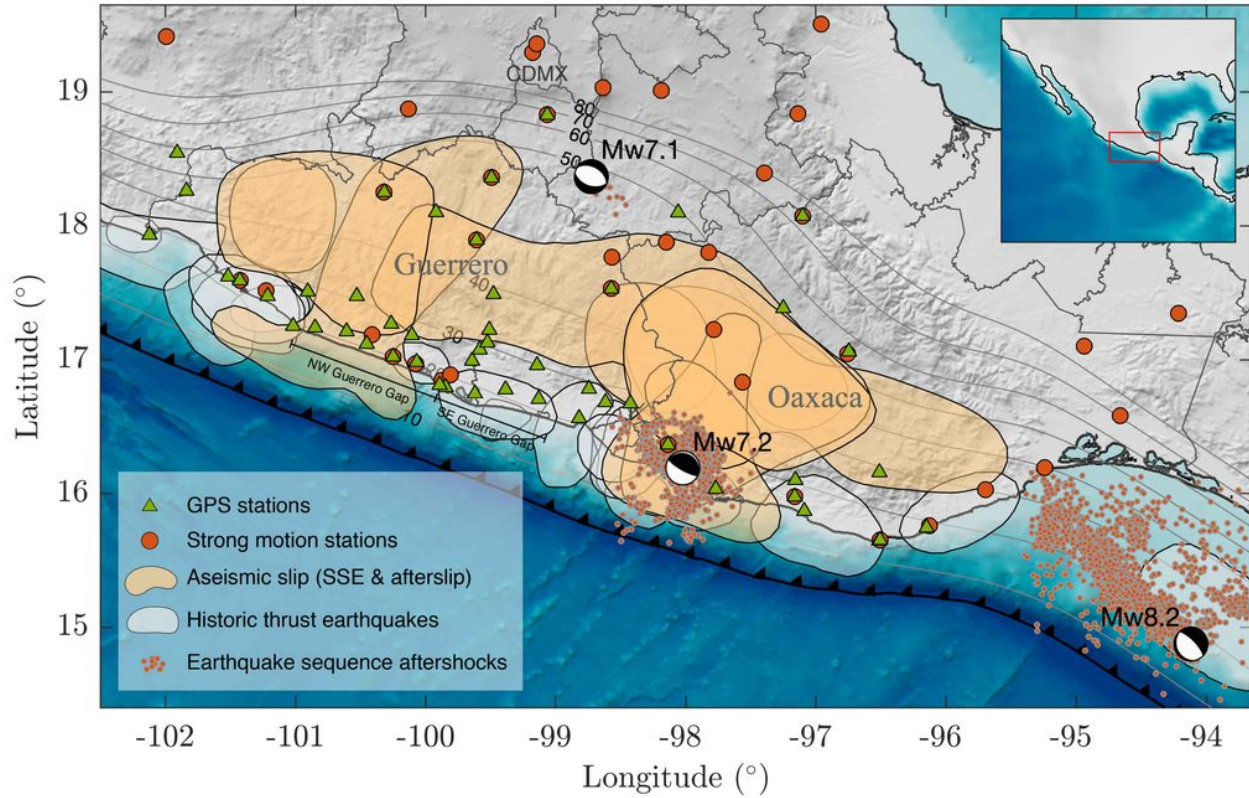


**Figure 1**

Study region and instrumentation where the Tehuantepec (Mw8.2), Puebla-Morelos (Mw7.1) and Pinotepa (Mw7.2) earthquake sequence took place. Orange shaded areas depict the 1 cm aseismic slip contours imaged between June 2017 and July 2019 in the plate interface (gray contours). White shaded contours depict rupture areas of historic thrust earthquakes. Orange dots show the 10-days aftershock sequences as reported by the SSN except for the Mw7.1 earthquake, for which three-months aftershocks are reported.

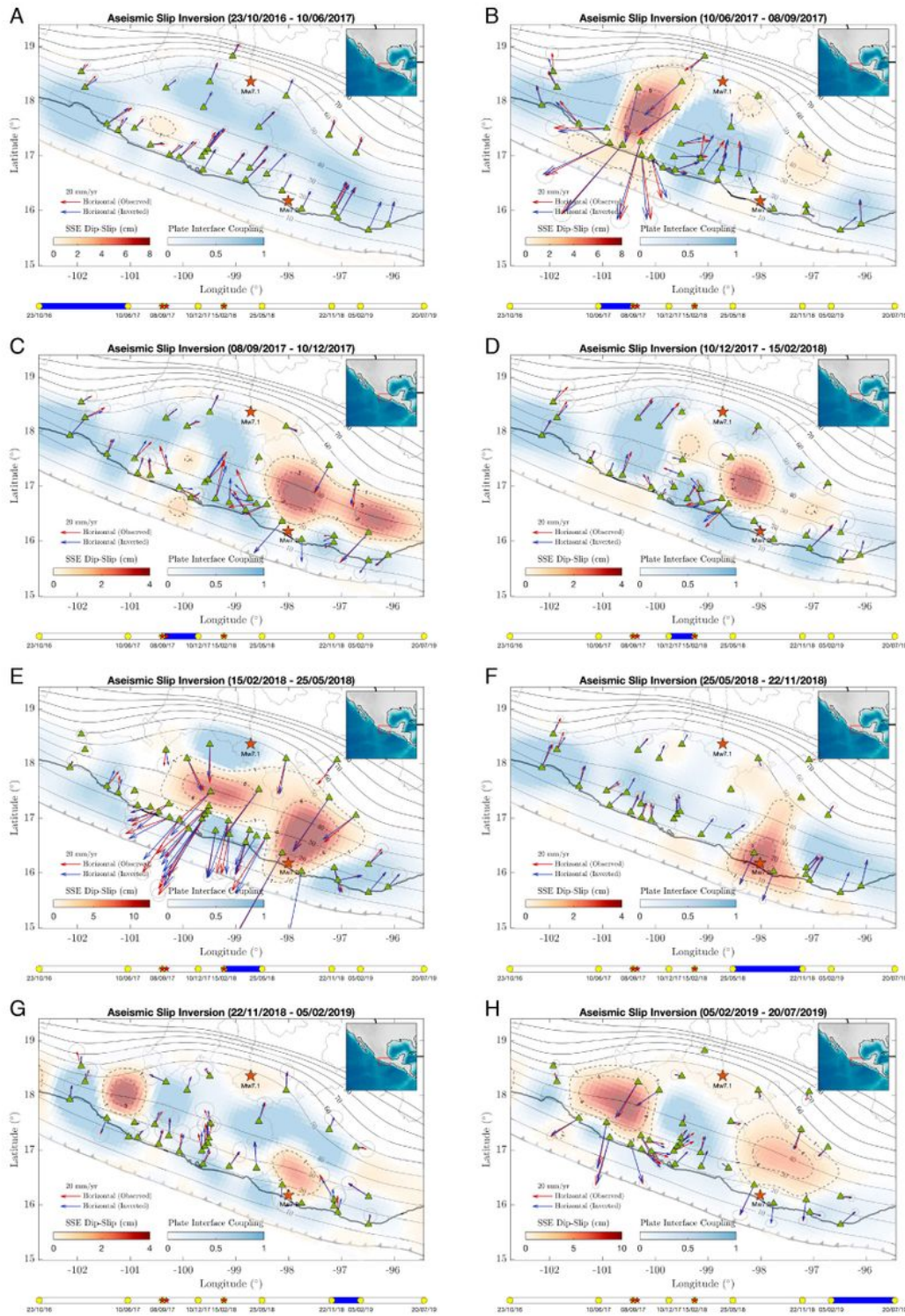


**Figure 2**

Aseismic slip inversion results for the whole analyzed period across and after the earthquake sequence. Dashed slip contours are in centimeters. Yellow circles encompassing the blue bar at the bottom of each panel indicate the dates of the associated inverted window, and red small stars, the Mw8.2 Tehuantepec, Mw7.1 Puebla-Morelos and Mw7.2 Pinotepa earthquakes timing, respectively, from left to right. Red and

blue arrows show the observed and synthetic surface displacements, and the gray ellipses one standard deviation of the GPS data.

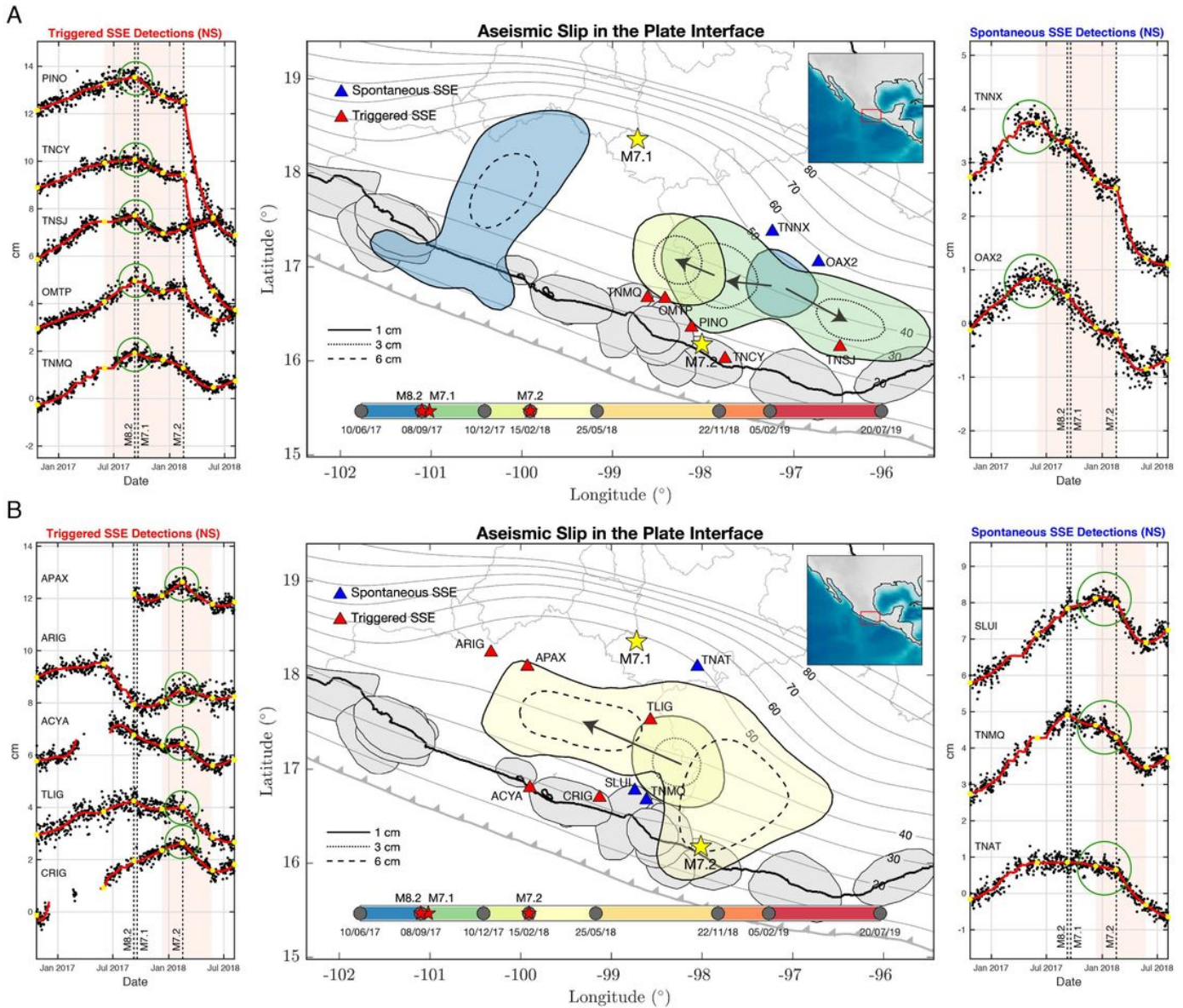


**Figure 3**

Evolution of the aseismic (SSEs and post-slip) during the earthquake sequence. Pink shaded rectangles encompass the associated inverted windows for each panel (yellow dots). Blue triangles show GPS stations where spontaneously initiated or preexistent SSE are observed (right panels, green circles), while red triangles show the stations where triggered SSE are detected (left panels, green circles). Notice the abrupt reversal of the deformation pattern (from north to south) right when the Tehuantepec and Pinotepa earthquakes happened in the left panels (green circles).

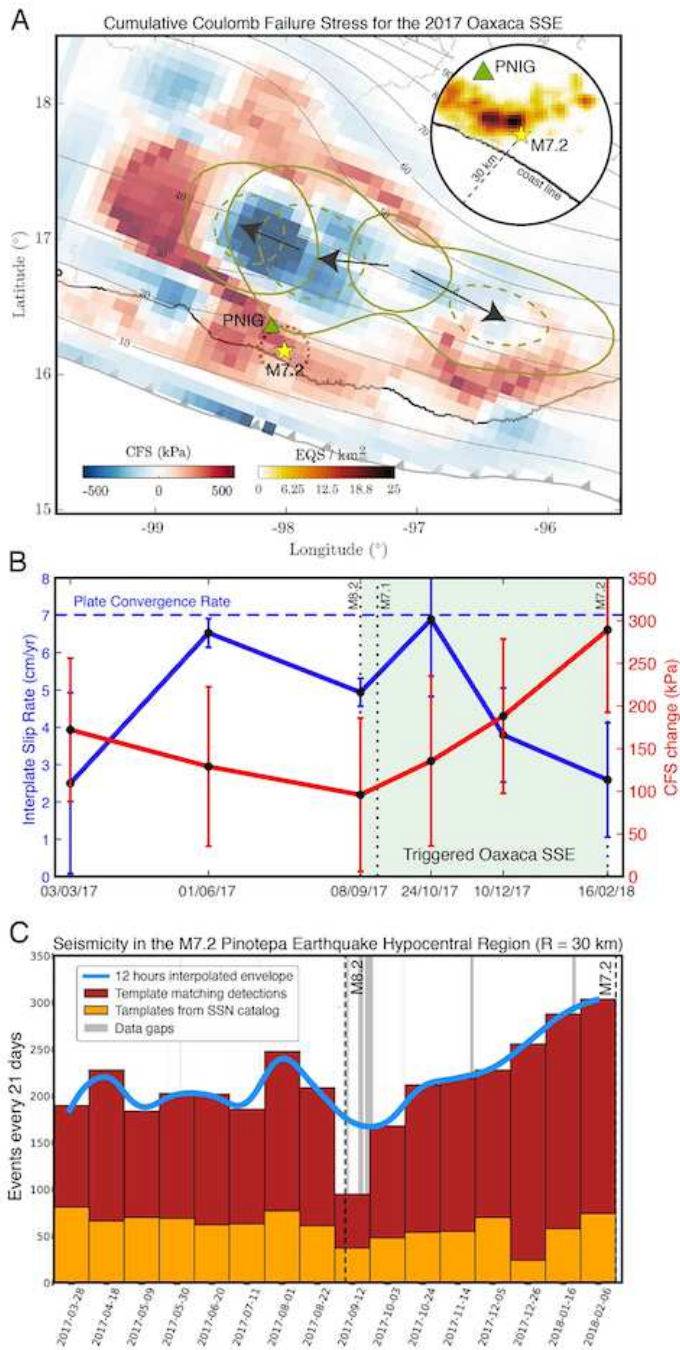


**Figure 4**

CFS, PIC and seismicity rate evolution before the Pinotepa earthquakes nearby its hypocenter. (A) 15-month cumulative CFS on the plate interface and spatial evolution of the 2017 Oaxaca SSE (1 cm slip solid contours and 3 cm slip dashed contours). Density of TM precursor detections (inset). (B) Temporal evolution of the CFS change and the interplate slip rate within a 20 km radius from the Pinotepa

earthquake hypocenter (dotted circle, panel A). See also Fig. S4. (C) Seismicity rate evolution for  $M > 2.1$  events within 30 km from the Pinotepa earthquake hypocenter.

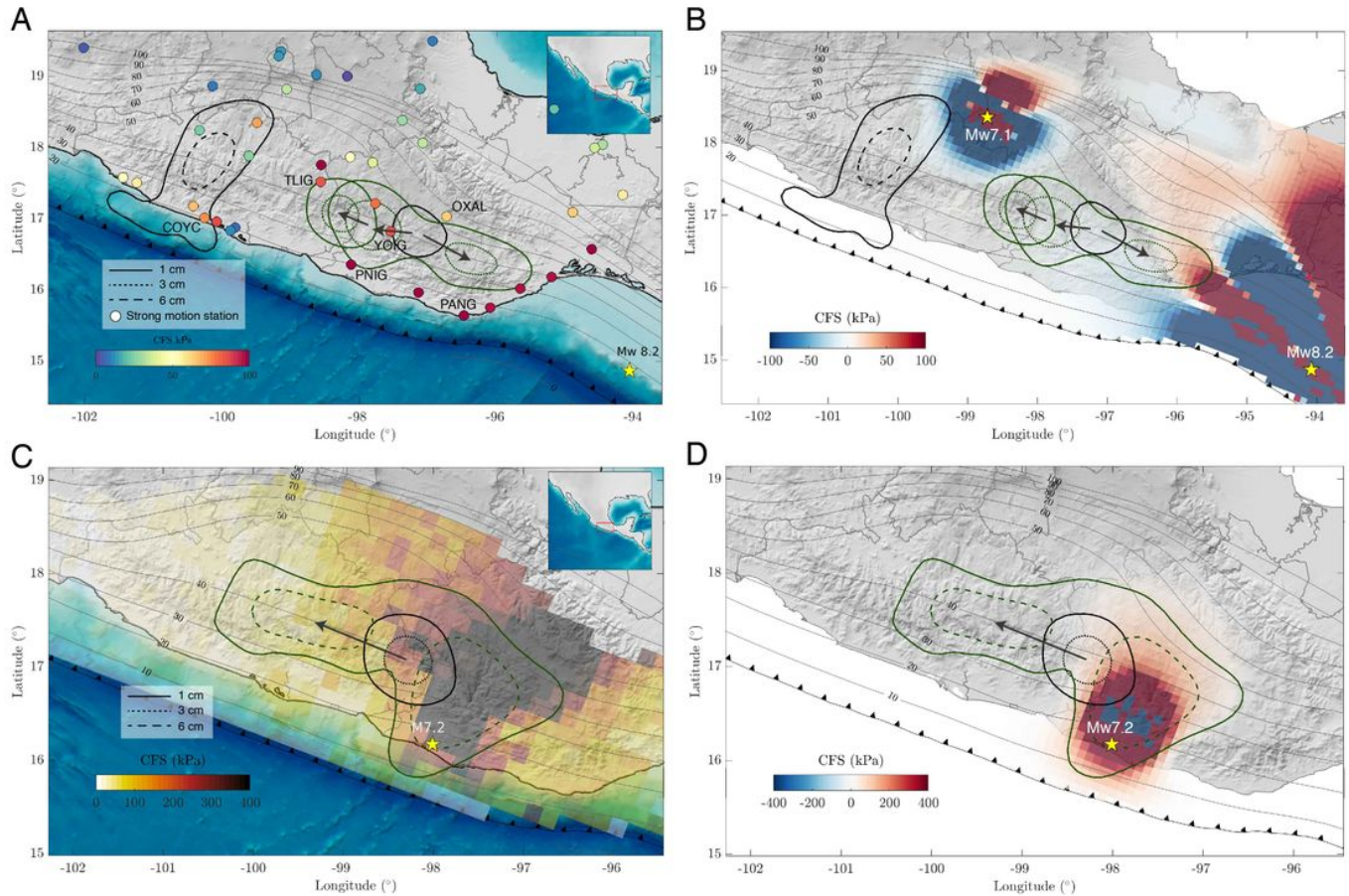


**Figure 5**

Dynamic (peak values) and static CFSs on the 3D plate interface (gray contours) produced by the Tehuantepec (A and B, respectively) and Pinotepa (C and D, respectively) earthquakes in the plate convergence direction. Aseismic slip events right before the corresponding earthquake are shown with black contours, while those occurred immediately after the earthquake are shown with green contours. Dynamic stresses for the Tehuantepec event (A) were computed from actual strong motion records at different sites (colored circles, see Fig. S8A). Estimates for the Pinotepa event (C) were computed through a 3D finite-source numerical simulation of the earthquake (see Fig. S9).

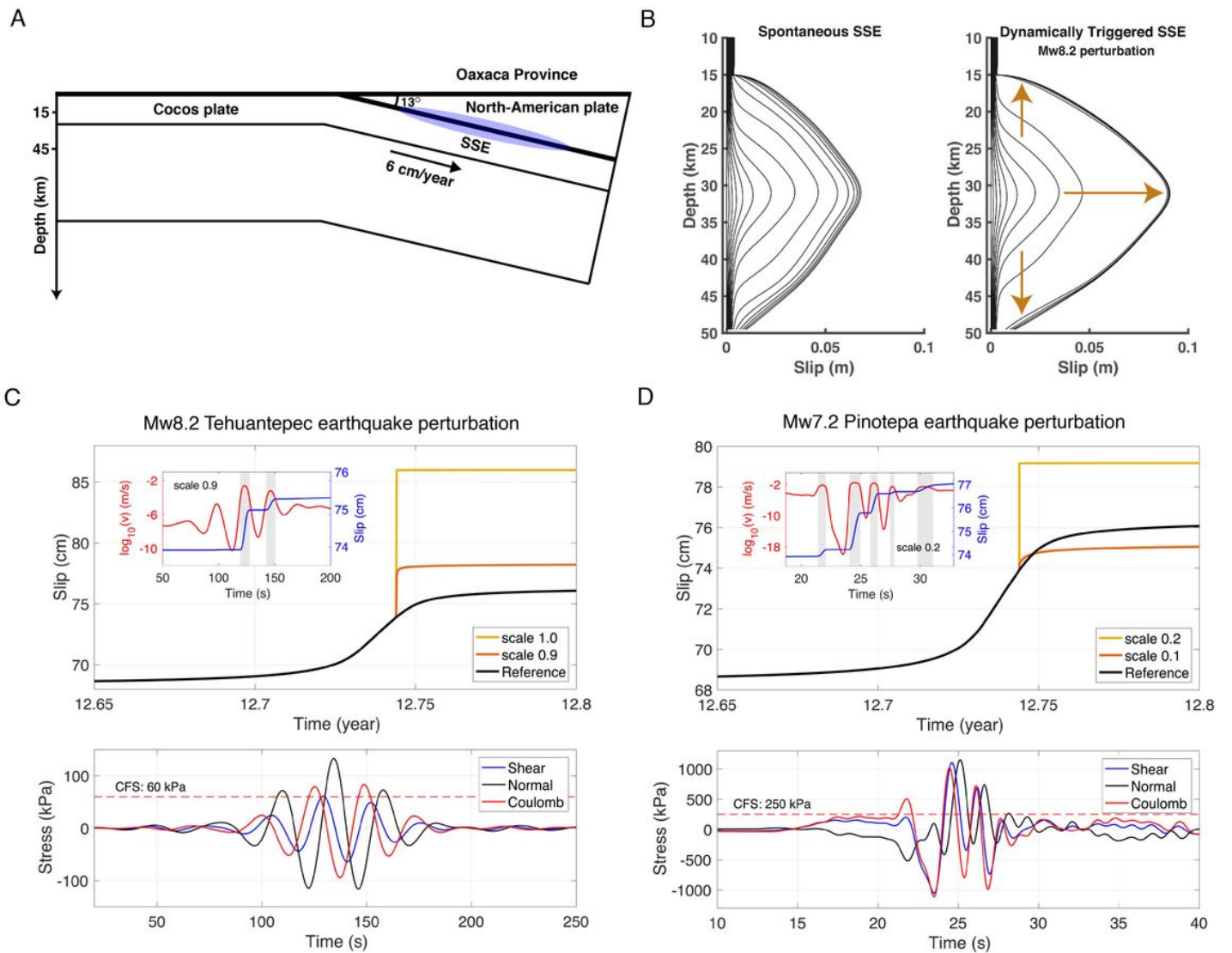


**Figure 6**

Rate-and-state fault model for SSE triggering by seismic-wave stress perturbations. (A) Synoptic 2-D model of the subduction zone in the study area. (B) Slip evolution of a spontaneous SSE and a dynamically triggered SSE in the rate-and-state friction model. The contours time increment is about 2 days. (C) Top, slip evolution of the SSE reference model and two triggered events at 31 km depth for stress perturbations due to the Mw8.2 Tehuantepec earthquake with different scaling factors. The inset shows the slip velocity and slip at that depth with 0.9 scaled perturbation. Bottom, stress perturbation used in these simulations. (D) Same as (C) but for the Mw7.2 Pinotepa earthquake. Please note that the scaling factors are different.

## Supplementary Files

This is a list of supplementary files associated with this preprint. Click to download.

- [CruzAtienzaetalNatComm2020SupplementaryMaterials.pdf](#)